

Myrmekite and strain weakening in granitoid mylonites

Alberto Ceccato^{1*}, Luca Menegon², Giorgio Pennacchioni¹, Luiz Fernando Grafulha Morales³

¹ Department of Geosciences, University of Padova, 35131 Padova, Italy

² School of Geography, Earth and Environmental Sciences, University of Plymouth, PL48AA Plymouth, UK

5 ³ Scientific Centre for Optical and Electron Microscopy (ScopeM) - ETH Zürich, Switzerland

Correspondence to: Alberto Ceccato (alberto.ceccato.2@phd.unipd.it)

* Now at: School of Geography, Earth and Environmental Sciences, University of Plymouth, PL48AA Plymouth, UK

Abstract. At mid-crustal conditions, deformation of feldspar is mainly accommodated by a combination of fracturing, dissolution/precipitation and reaction-weakening mechanisms. In particular, K-feldspar is reaction-weakened by formation of strain-induced myrmekite - a fine-grained symplectite of plagioclase and quartz. Here we use EBSD (i) to investigate the microstructure of a granodiorite mylonite, developed at ~ 450 °C during cooling of the Rieserferner pluton (Eastern Alps), and (ii) to assess the microstructural processes and the weakening associated with myrmekite development. Our analysis shows that the crystallographic orientation of plagioclase in pristine myrmekite was controlled by that of the replaced K-feldspar. Myrmekite nucleation resulted in both grain size reduction and anticlustered phase mixing by heterogeneous nucleation of quartz and plagioclase. The fine grain size of sheared myrmekite promoted grain size-sensitive creep mechanisms including fluid-assisted grain boundary sliding in plagioclase, coupled with heterogeneous nucleation of quartz within creep cavitation pores. Flow laws, calculated for monomineralic quartz, feldspar, and quartz + plagioclase aggregates (sheared myrmekite) during deformation at 450 °C, show that grain-size-sensitive creep in sheared myrmekite accommodated strain rates several orders of magnitude higher than monomineralic quartz layers deforming by dislocation creep. Therefore, diffusion creep and grain size-sensitive processes contributed significantly to bulk rock weakening during mylonitization. Our results have implications for modelling the rheology of the felsic middle crust.

25 1. Introduction

Localization of ductile strain within rocks arises from weakening associated with grain size refinement processes by dynamic recrystallization, metamorphic reactions, and microfracturing (e.g. Platt et al., 2015, and reference therein). Grain size reduction, accompanied by phase mixing in polymineralic rocks at high strains, commonly results in a switch of deformation mechanism from grain-size-insensitive (GSI) to grain-size-sensitive (GSS) creep – one of the most effective strain weakening mechanisms within shear zones (Kruse and Stünitz, 1999; Kilian et al., 2011; Menegon et al., 2013).

Feldspars locally form the load-bearing framework of crustal rocks (Handy, 1994). At mid-crustal conditions, feldspar deformation mainly occurs by microfracturing and dissolution/precipitation processes, typically associated with metamorphic reactions (Behrmann and Mainprice, 1987; Michibayashi, 1996; Stünitz and Tullis, 2001; Gueydan et al., 2003; Ree et al., 2005). Kfs (K-feldspar –
5 mineral abbreviations in the text are according to Kretz, 1983) is commonly replaced by myrmekite –
a fine-grained symplectic aggregate of Qtz (quartz) and Plg (plagioclase) (Becke, 1908; Vernon, 1991). Myrmekite replacement is either related to Kfs chemical instability (Cesare et al., 2002), in some cases involving local metasomatic fluids (Phillips, 1980), or triggered by stress concentration and intracrystalline strain in Kfs during deformation (Simpson and Wintsch, 1989; Menegon et al., 2006).
10 This replacement is acknowledged as a weakening mechanism during ductile deformation of granitoid rocks (LaTour and Barnett, 1987; Simpson and Wintsch, 1989; MacCaffrey, 1994; O'Hara et al., 1997; Tsurumi et al., 2003; Pennacchioni, 2005; Menegon et al., 2006; Pennacchioni and Zucchi, 2013; De Toni et al., 2016). Deformation and shearing of myrmekite result in a fine-grained Plg + Qtz aggregate, that is manifestly weaker than original coarse Kfs (Tsurumi et al. 2003; Ree et al., 2005; Ciancaleoni and Marquer, 2006). In general, a fine grain size and the local presence of grain boundary aqueous fluid promote phase mixing and the development of ultramylonites (Vernon, 1991; Kilian et al., 2011; Czaplínska et al., 2015). Though the key role of myrmekite in strain localization has been recognized, it has not been accompanied with a quantitative analysis of the deformation mechanisms within myrmekite-derived, fine-grained Plg + Qtz aggregates.
20 Here we present a detailed analysis of myrmekite evolution, from the nucleation stage within Kfs to the development of sheared Plg + Qtz aggregates, and of the associated rheological weakening that resulted in strain localization in the mylonites of the Rieserferner granitoid pluton (Eastern Alps). In this pluton, ductile shear zones nucleated along joints that were locally filled with Qtz and Ep (epidote) veins during post-magmatic cooling (Ceccato et al., 2017; Ceccato and Pennacchioni, 2018). The
25 progressive development of granodiorite mylonite was associated with consumption of Kfs by myrmekite leading to increasingly interconnected, fine-grained Plg + Qtz layers. Microstructures of granodiorite mylonite have been analysed to characterize: (i) the process of myrmekite nucleation; (ii) the deformation mechanisms during myrmekite shearing and transition to Plg + Qtz aggregates; (iii) the deformation mechanisms of pure Qtz layers; (v) the deformation mechanisms of Kfs porphyroclasts
30 and of Kfs new grains during mylonitization. Furthermore, the application of mixed flow laws of the aforementioned deformation mechanisms for polymineralic aggregates allows the degree of rheological weakening resulting from deformation of myrmekite to be quantified.

2. Geological setting and field description

The tonalitic-granodioritic Rieserferner pluton (Eastern Alps) (Bellieni, 1978) was emplaced at ~15 km depth (0.4 GPa; Cesare et al., 2010) into the Austroalpine nappe system at 32 Ma (Romer and Siegesmund, 2003). During post-magmatic cooling, a main set of ductile shear zones exploited shallowly ESE-dipping joints, and the joint-filling Qtz and Ep veins (Ceccato, 2018; Ceccato and Pennacchioni, 2018). The temperature of ductile shearing has been estimated at 420-460 °C based on thermodynamic modelling (Ceccato, 2018). Ductile shearing along joints and Ep-filled joints resulted in cm-thick heterogeneous shear zones with a sigmoidal-shaped foliation in the host granodiorite (Ceccato and Pennacchioni, 2018) likely reflecting fluid-rock interaction at the vein selvages (Pennacchioni and Mancktelow, 2018). In contrast, Qtz veins filling the joints sharply localized homogeneous shearing (Ceccato et al., 2017).

3. Analytical methods

Polished thin sections of granodiorite mylonite were prepared for the study of the microstructure and of the crystallographic preferred orientations (CPO). The thin sections were made from rock chips cut parallel to the stretching lineation and perpendicular to the shear plane (XZ plane of finite strain ellipsoid).

Electron backscattered diffraction analysis was carried out on a JEOL 7001 FEG SEM equipped with a NordLys Max EBSD detector (AZTec acquisition software, Oxford Instruments) at the Electron Microscopy Centre of Plymouth University. EBSD patterns were acquired on rectangular grids with step sizes of 0.2, 0.3 and 0.35 μm . Working conditions during acquisition of EBSD patterns were 20 kV, 70° sample tilt, high vacuum, and working distance between 17 and 23 mm. A detailed description of the EBSD post-processing methods and of the image analysis are reported in Appendix A. The microstructural and CPO analysis conducted with EBSD were complemented with cathodoluminescence (CL) and microchemical analyses.

CL imaging was performed in a FEI Quanta 200 FEI equipped with Gatan monacle detector. Imaging was performed using an accelerating voltage of 20 kV, beam current of 8 nA and working distance of 20 mm in C-coated (15 nm) thin sections used for EBSD analysis. To avoid incorrect interpretation of potential artefacts in the sample, secondary (SE) and backscatter electron images were collected simultaneously with CL.

Microchemical analyses were performed with EM wavelength-dispersive spectroscopy (WDS) at Electron Microprobe Laboratory at the Università degli Studi di Milano with a Jeol 8200 Super Probe; the operating conditions were: 15 kV accelerating voltage; 5 nA (Kfs and Plg) beam current. PAP correction program was applied to convert X-ray counts into oxide weight percentages.

5 4. Microstructure

The Rieserferner granodiorite consists of Qtz, Plg, Kfs, Bt (biotite), Ep, Hbl (hornblende), Ap (apatite), and Ttn (titanite). The magmatic Plg displays normal oscillatory zoning ($An_{58} - An_{32}$). Plg crystals are arranged in glomeroclasts, included in Kfs ($Or_{93}Ab_7$). Various grain-size reduction mechanisms accompanied the development of a mylonitic foliation in the granodiorite: (i) recrystallization of Qtz and Bt (Fig. 1a,b); (ii) formation of myrmekite after Kfs (Fig. 1c,d); (iii) microfracturing of feldspar; and (iv) formation of Plg ($An_{29}Ab_{71}Or_{<1}$) + Ttn + Wmca (White Mica) symplectite at Bt-Plg boundaries (Pennacchioni et al., 2006; Johnson et al., 2008). Pristine myrmekite make a transition to fine grained aggregates of dominant Plg + Qtz extending into the foliation (Fig. 1b,e). The mylonitic foliation is defined by alternating layers of: (i) monomineralic Qtz; (ii) Plg ($An_{26}Ab_{74}Or_{<1}$) + Qtz + Kfs; and (iii) Bt and recrystallized Bt/Plg (Fig. 1a). Syn-kinematic Kfs neoblasts ($Or_{96}Ab_4$) are found in strain shadows around porphyroclasts and dilatant fractures, and are in turn locally replaced by myrmekite (Fig. 1d).

With increasing strain, the volume percentage of Kfs decreases from 19 vol% (undeformed rock and protomylonite), to 1-6 vol% (rare scattered porphyroclasts in mylonite and ultramylonite) (Fig. 2). As counterbalance, the volume percentage of fine-grained myrmekite and derived Plg + Qtz aggregates, increases from 3 vol% (undeformed rock and protomylonite) to as much as 13 vol% (mylonite and ultramylonite) (Fig. 2). Ultramylonites consist of a fine-grained (ca. 10 μm grain size) well-mixed matrix of Qtz, Plg, Bt, Ep, Kfs, Ttn, Ap \pm Grt (Garnet) \pm Wmca.

5. EBSD and cathodoluminescence analysis

25 5.1 Pristine myrmekite

Pristine myrmekite shows: (i) preferential development along grain boundaries of Kfs porphyroclast oriented parallel to the mylonitic foliation (Fig. 1b-e); (ii) lobate shape protruding into the Kfs (Fig. 1c); (iii) single grain structure of Plg within each lobe, embedding vermicular Qtz; (iv) rather constant spacing of Qtz vermicules of about 3-5 μm across the entire lobe; and (v) preferential elongation of the Qtz vermicules orthogonal to the myrmekite/Kfs boundary.

The EBSD analysis shows that: (i) Kfs and myrmekitic Plg commonly have similar crystallographic orientations ($(100)_{\text{Kfs}} \parallel (100)_{\text{Plg}}$, $(010)_{\text{Kfs}} \parallel (010)_{\text{Plg}}$, and $(001)_{\text{Kfs}} \parallel (001)_{\text{Plg}}$; Fig. 3b, c); (ii) Qtz vermicules do not share any crystallographic plane or direction with Kfs or myrmekitic Plg (Fig. 3b-c-d); (iii) Qtz vermicules do not show any obvious CPO, but they usually have similar crystallographic orientation within a myrmekite lobe (see encircled clusters in Fig. 3d) (Abart et al., 2014); and (iv) Dauphiné and Albite twins are occasionally observed in Qtz and Plg, respectively.

The Plg of myrmekite lobes exhibits rare low angle boundaries (misorientations $>2^\circ$, $>5^\circ$) that abut against the Qtz vermicules (Figs. 3a and 4a). The internal distortion of myrmekitic Plg is very small ($<1^\circ$; Fig. SOM1a).

10 5.2 Sheared myrmekite: plagioclase + quartz aggregates

Plg + Qtz aggregates (\pm rare Kfs and Bt) wrap around Kfs porphyroclasts and are elongate into the foliation (Fig. 1e). These aggregates make transition to, and extend into the foliation from, pristine myrmekite and are hereafter referred to as sheared myrmekite.

Qtz grains in sheared myrmekite occur either as isolated single grains at triple/quadruple junctions between Plg grains or, less commonly, as polycrystalline aggregates elongated normal to the foliation (Fig. 4a). Qtz grains within sheared myrmekite have no CPO (Fig. 4b), show little internal distortion and show rare low angle boundaries with scattered misorientation axis distribution (Fig. 4c). Misorientation angle distribution for correlated pairs displays higher frequency than a random-pair distribution for misorientations $< 15^\circ$ and at 60° (Fig. 4d). The uncorrelated misorientation angle distribution approaches the random-pair distribution.

Plg grains do not show any obvious CPO (Fig. 4e), and display little internal distortion and rare low angle boundaries. The low and high angle misorientation axes in crystal coordinate system are almost uniformly distributed (Fig. 4f). Even though very close to random-pair distribution, correlated misorientation distribution exhibits two distinct peaks at very low angles ($<5-10^\circ$) and close to 180° (Fig. 4g). Misorientations $<70^\circ$ occurs with slightly higher frequency than the random-pair distribution. Albite-twins and related 180° misorientations are rarely observed inside new grains (Figs. 3a-4a). In CL both myrmekitic Plg and Qtz have a grey shade similar to the surrounding non-myrmekitic Plg and Qtz (similar to Hopson and Ramseyer, 1990) (Fig. 1f,h).

5.3 K-feldspar aggregates in strain shadows

In this section, EBSD data are used to describe the relationship between Kfs neoblasts and porphyroclasts. Kfs neoblasts occur in strain shadows around feldspar porphyroclasts, as well as dispersed within the sheared myrmekite (Figs. 3a, Area C in Fig. 4a; Fig. SOM2). In strain shadows, the orientation of (100), (010) planes and [001] direction of the neoblasts is similar to that of the porphyroclast (Fig. 4h-j). In particular, the Kfs neoblasts show a CPO for (010) planes close to the Y kinematic axis (Fig. SOM2d), which is similar to the orientation of (010) in the adjacent porphyroclast. Misorientation axis/angle distributions show very few scattered data without any clear clustering (Fig. 4k). The grain size of new Kfs grains dispersed within sheared myrmekite is ca. 7 μm , comparable to that of the Plg in the surrounding sheared myrmekite (Fig. 5l).

The CL imaging of Kfs highlights a complex microstructure, which is different between new grains and porphyroclasts. The porphyroclasts show a homogeneous bright shade overprinted by a complex low-grey CL shade (Fig. SOM3). Kfs grains in sheared myrmekite and tails around porphyroclasts show a homogeneous low-grey CL shade (Fig. SOM3). Kfs aggregates elongated parallel to the foliation and enveloped by sheared myrmekite are characterized by bright irregularly-shaped Kfs cores (porphyroclasts) surrounded by low-grey shaded Kfs.

5.4 Quartz layers along foliation

Monomineralic Qtz layers defining the mylonitic foliation (Figs. 3, 4 and 5) show a variable grain size, and a shape preferred orientation (SPO) inclined to the foliation consistently with the sense of shear. Dauphiné twin boundaries are widespread (red boundaries in Fig. 5a). The Qtz c-axis CPO defines an asymmetric Type-II girdle roughly normal to the local mylonitic foliation (Fig. 5b). The pole figures of c-axis and $\langle a \rangle$ directions show maxima close to the Y and to the X kinematic directions, respectively. Misorientation axis distribution for low angle misorientation ($<10^\circ$) exhibits a wide maximum close to c-axis and $\langle \pi-\pi' \rangle$ directions in crystal coordinates. These misorientation axes preferentially cluster close to (but slightly off-set from) the Y-kinematic direction in sample coordinates (Fig. 5c). High angle misorientation axis distributions do not show any clear systematic pattern, except for misorientations around 60° . Misorientation angle distribution (Fig. 5d) shows two peaks at very low angle misorientations ($<10^\circ$) and around 60° for correlated misorientations. Uncorrelated misorientation angle distribution is close to the random-pair distribution. CPOs and misorientation data of coarser grains do not differ from those of finer grains. In CL images the Qtz layers display an overall homogeneous signature, with lower-grey shades close to inclusions and layer boundaries (Fig. SOM3).

6. Phase spatial distribution, grain size and aspect ratio

The results of image analysis of EBSD phase maps indicate that pristine and sheared myrmekite have the same phase ratio with ca. 18 vol% of Qtz. We have analysed the phase spatial distribution of Plg and Qtz in both pristine and sheared myrmekite to define their deviation from a random distribution, either towards a clustered or an anticlustered distribution (Heilbronner and Barrett, 2014). Phase spatial distribution analysis of a two-phase aggregate compares the cumulative lengths of phase boundaries (boundaries between grains of a different phase) and of grain boundaries (boundaries between grains of the same phase) with those expected for a random distribution of the two phases. We have considered three types of boundaries: (i) Plg – Plg grain boundaries; (ii) Qtz – Qtz grain boundaries; and (iii) Plg – Qtz phase boundaries. The results (Fig. 6) show that, in pristine and sheared myrmekite: (i) the surface area fraction of Qtz ranges between 0.55-0.75 and 0.55-0.65, respectively; (ii) Qtz – Qtz grain boundaries occur with a lower probability than for a random distribution, indicative of an anticlustered distribution; (iii) Plg – Plg grain boundaries occur with a higher probability than for a random distribution indicative of a more clustered distribution; and (iv) Plg + Qtz aggregates display an anticlustered distribution, with Plg – Qtz phase boundaries occurring with higher probability than for random distribution of phases.

Grain size distributions for Qtz (Fig. 7) and Plg (Fig. 8) are quite different for pristine myrmekite, sheared myrmekite and in monomineralic Qtz layers. In pristine myrmekite, large single grains of Plg (20-50 μm , Fig. 8a) embed Qtz vermicules $\sim 3 \mu\text{m}$ in equivalent diameter (Fig. 7a). In sheared myrmekite, Qtz grain size is around 3 μm (Area B in Fig. 4a; Fig. 7b), but locally increases to $>10 \mu\text{m}$ (Area C in Fig. 4a; Fig. 7c); individual Qtz grains show polygonal, equant shapes (aspect ratio AR, ratio of long to short axis; $1.5 < \text{AR} < 1.75$; Fig. 7e) or a weak shape preferred orientation (SPO) oriented at low angle to the local mylonitic foliation (Fig. 7e). Plg grains (average grain size of about 7 μm : Figs. 8b-c) are mainly polygonal and range in shape from almost equant to elongated ($1.75 < \text{AR} < 2$; Fig. 8d). Elongated grains define an SPO almost parallel to the local mylonitic foliation (Fig. 8d for Area B in Fig. 4a).

Monomineralic Qtz layers along the foliation show a variable grain size, usually ranging between 10 μm and 120 μm , mimicking a bimodal grain size distribution with maxima centred respectively at 20-35 μm and 50-70 μm (Figs. 7d and SOM4). The coarser grain size ($>40 \mu\text{m}$) is observed close to the centre of Qtz layers. These grains are usually characterized by subgrains ranging in size between 20 and 35 μm . The smaller grain size ($<40 \mu\text{m}$) commonly envelopes the coarser grains, in addition to

prevail at the boundary between monomineralic Qtz layers and sheared myrmekite, or around feldspar porphyroclasts (Figs. 3, 4 and SOM4e).

7. Discussion

7.1 Formation and shearing of myrmekite

5 7.1.1 Crystallographic relationship between K-feldspar and myrmekitic phases

The EBSD analysis indicates that the Kfs and the overgrowing myrmekitic Plg have a similar crystallographic orientation, though with some scattering (Fig. 3b; Wirth and Voll, 1987). This suggests the occurrence of a topotactic replacive process where $(100)_{\text{Kfs}} \parallel (100)_{\text{Plg}}$, $(010)_{\text{Kfs}} \parallel (010)_{\text{Plg}}$, and $(001)_{\text{Kfs}} \parallel (001)_{\text{Plg}}$. The scatter in crystallographic orientation between Kfs and myrmekitic Plg is interpreted to result from deformation during and after myrmekite formation (see section 6.1.2). The crystallographic orientation of myrmekitic Plg and Qtz was not controlled by neighbour Plg or Qtz grains previously in contact with the Kfs, differently from what is reported by other authors (Stel and Breedveld, 1990; Abart et al., 2014). As observed by Abart et al. (2014), the different myrmekite Qtz vermicules have a similar crystallographic orientation. The anticlustered phase spatial distribution of pristine myrmekite is related to the process of heterogeneous phase nucleation during myrmekite formation (Wirth and Voll, 1987).

7.1.2. Transition from pristine- to sheared myrmekite (plagioclase + quartz aggregates)

The sheared Plg + Qtz aggregates, wrapping Kfs porphyroclasts and elongated into the foliation, resulted from shearing of pristine myrmekite. The transition from pristine to sheared myrmekite was a dynamic process and here we try to constrain the processes involved as inferred from microstructural changes. These microstructural changes included: (i) randomization of Plg CPO observed in pristine myrmekite; (ii) evolution of Plg grain size distribution from heterogeneous (ranging between 3 to 50 μm) in pristine myrmekite, to homogeneous and centred at 7 μm in sheared myrmekite (Figs. 3, 4 and 8a); (iii) coarsening of Qtz grains from $<3 \mu\text{m}$ thick vermicules to rounded-to-polygonal grains as large as 10 μm in sheared myrmekite (Fig. 7). The processes of grain size evolution are probably related to the minimization of interfacial energy in the vermicular microstructure of pristine myrmekite (e.g. Odashima et al., 2007; Dégi et al., 2010). Qtz grain coarsening reflects annealing of the pristine vermicular microstructure after the reaction front moved further into the Kfs (Fig. 3a), and was probably aided by dissolution-precipitation processes. Qtz coarsening implies simultaneous grain size refinement of Plg, which probably involved microfracturing, with the development of local microcracks in myrmekitic Plg. Misorientation analysis on the few low and high misorientation angle

boundaries inside pristine myrmekite (inside myrmekitic Plg) shows abrupt misorientations of as much as 8° across such boundaries, which could be interpreted as either micro-cracks or growth features considering the low internal distortion of grains (Figs. 3, SOM1). Microfractures could have originated from stress concentrations within the 3-D geometrically/mechanically composite structure of myrmekite (see figure 2 of Hopson and Ramseyer, 1990; Dell'Angelo and Tullis, 1996; Xiao et al., 2002). Therefore, the Plg grain size in the incipiently-sheared aggregate may be controlled by the spacing between Qtz vermicules in pristine myrmekite. Myrmekite were then sheared along the mylonitic foliation from the contractional sites around the Kfs porphyroclast. Then, interconnected layers of sheared myrmekite developed from foliation-parallel stretching of isolated myrmekite mantling Kfs during mylonitization (similar to Boullier and Gueguen, 1975).

7.2. Deformation mechanisms in the Rieserferner mylonites

7.2.1. Sheared myrmekite

Plg and Qtz of sheared myrmekite both display: (i) a weak CPO; (ii) rare low angle boundaries without systematic pattern of misorientation axis distribution; and (iii) correlated and un-correlated misorientation angle distributions close to the theoretical random-pair distribution. All these features suggest very limited dislocation creep in both minerals (Kruse et al., 2001; Okudaira and Shigematsu, 2012; Miranda et al., 2016). In addition, sheared myrmekite show: (i) fine-grained Plg and Qtz with polygonal, equant to slightly elongated shape ($AR < 2$); (ii) aligned grain boundaries (over the scale of several grain diameters) and common triple/quadruple-junctions; and (iii) anticlustered spatial distribution of Plg and Qtz. These microstructural features are consistent with GSS creep, including fluid-assisted grain boundary sliding (GBS) (Boullier and Gueguen, 1975; White, 1977; Stünitz and Fitz Gerald, 1993; Fliervoet et al., 1997; Jiang et al., 2000; Wheeler et al., 2001; Lapworth et al., 2002; Bestmann and Prior, 2003; Kilian et al., 2011; Menegon et al., 2013).

Phase spatial distribution in deformed bimodal aggregates in mylonites is interpreted to reflect the activity of specific deformation mechanisms (Kruse and Stünitz, 1999; Menegon et al., 2013). In particular, diffusion creep in polymineralic aggregates is commonly accompanied by heterogeneous phase nucleation that promotes phase mixing and a high degree of anticlustering in phase distribution (Kilian et al., 2011; Menegon et al., 2013). The occurrence of Qtz in triple-quadruple junctions and Qtz aggregates elongated orthogonal to the foliation in sheared myrmekite suggest creep cavitation and heterogeneous Qtz nucleation during GSS creep of Plg (Fusseis et al., 2009; Herwegh et al., 2011; Kilian et al., 2011). Heterogeneous phase nucleation in creep cavities led to the anticlustered phase

spatial distribution (Fig. 6) (Hiraga et al., 2013; Menegon et al., 2015). The constant Plg grain size of sheared myrmekite may then result from the combination of initial spacing between Qtz vermicules in pristine myrmekite, diffusion creep processes and second-phase grain-boundary pinning during shearing (Herwegh et al., 2011). GSS processes, phase mixing and second-phase grain-boundary pinning inhibit grain growth and stabilizes grain size, hindering the efficiency of dynamic recrystallization processes and self-sustaining the activity of GSS processes.

7.2.2. K-feldspar tails and neoblasts

Kfs is abundant in the low-strain portions of the mylonite (Fig. 2). Kfs porphyroclasts and tails do not show any CPO or misorientation axis distribution referable to dislocation creep processes (Figs. 4i, SOM2; Menegon et al., 2008, and reference therein). The similar crystallographic orientation between feldspar(s) porphyroclasts and either Kfs tails or fine neoblast aggregates can be explained invoking epitaxial nucleation and growth during dissolution – precipitation (Figs. 4, SOM2). Dissolution – precipitation would be consistent with the Kfs aggregate microstructure observed under CL, which probably reflect either the different chemistry, or the different intragranular strain, observed between magmatic (Or₉₃Ab₇) and synkinematic Kfs (Or₉₆Ab₄) (Shimamoto et al., 1991; Ramseyer et al., 1992; Götze et al., 1999; Słaby et al., 2008, 2014). The modification of the inherited CPO in fine-grained aggregates could be then related to the occurrence of anisotropic dissolution – precipitation processes and grain boundary sliding during myrmekite shearing (Behrmann and Mainprice, 1987; Menegon et al., 2008, 2013).

7.2.3. Monomineralic quartz layers

The microstructures, CL signatures and strong crystallographic preferred orientation of monomineralic Qtz layers indicate deformation by dominant dislocation creep aided by subgrain rotation (SGR) recrystallization (e.g. Fliervoet et al., 1997; Wheeler et al., 2001; Stipp et al., 2002; Bestmann and Pennacchioni, 2015). The misorientation axes distributions suggest the preferential activation of {m}<a> and {r-z}<a> slip systems (e.g. Ceccato et al., 2017 and references therein).

The analysis of the grain orientation spread (GOS), to distinguish different generation of relict and/or recrystallized grains (Cross et al., 2017), suggests that there are no meaningful correlations between grain size and average grain distortion. This missing correlation may reflect a non-steady-state Qtz microstructure during a prolonged deformation history or, more likely, the development of the microstructures at different temperature conditions during pluton cooling. The bimodal grain size of recrystallized Qtz includes coarser grains that we infer developed during the relatively high-

temperature bulk solid-state deformation of the host granodiorite predating the development of localized shear zones at 450 °C dominated by SGR recrystallization (Ceccato et al., 2017; Ceccato and Pennacchioni, 2018). Coarser grains in Qtz layers (grain sizes from >40) record differential stresses < 40 MPa and strain rates of $10^{-13} - 10^{-14} \text{ s}^{-1}$ as retrieved applying the grain size paleopiezometer of Cross et al. (2017). Subgrain and finer grains (20-35 μm in diameter) suggest that localized deformation and shearing occurred at differential stresses close to 40-70 MPa and strain rates of $10^{-11} - 10^{-12} \text{ s}^{-1}$ (Stipp and Tullis, 2003; Cross et al., 2017).

7.3. The rheology of the Rieserferner mylonites

The rheological effect of transformation of coarse Kfs to fine-grained sheared myrmekite and the transition to an interconnected, weak, fine-grained microstructure (Handy, 1990) is estimated here by investigating the deformational behaviour of different mixtures of Plg and Qtz, in which deformation is accommodated either by dislocation creep or by diffusion creep. Our simplified model does not include Bt, Wmca and Bt + Plg aggregates. Based on the deformation mechanisms identified from the microstructural analysis, deformation mechanisms maps have been calculated and plotted on grain-size vs. differential stress and on differential-stress vs. strain rate diagrams for the following three end-member compositions (Fig. 9):

- (i) monomineralic Qtz layer deforming via both dislocation and diffusion creep (Fig. 9a);
- (ii) sheared myrmekite, modelled as 80 vol% Plg (An_{60}) + 20 vol% Qtz deforming via both dislocation creep and grain size sensitive creep (Fig. 9b); the input grain size is 7 μm , identical for both minerals;
- (iii) a mixture of 60% Plg (An_{100}) + 40% Qtz assumed as a simplified composition representative of a mica-free granitoid rock deforming only by dislocation creep (after referred as “granitoid”) (Fig.9c).

The flow law of Hirth et al. (2001) has been used to calculate the dislocation creep component in deformation mechanisms maps for Qtz:

$$(1) \dot{\epsilon} = A_q f_h \sigma^n e^{\left(-\frac{Q_q}{RT}\right)}$$

where: A_q is the pre-exponential factor for Qtz ($\text{MPa}^{-n} \text{ s}^{-1}$); f_h is the water fugacity; σ is the differential stress (MPa); n is the stress exponent; Q_q is the activation energy (J); R is the gas constant ($\text{J/K}^*\text{mol}$); T is the temperature (K). The contribution of pressure-solution creep in Qtz has been calculated following the flow law for thin-film pressure-solution of den Brok (1998):

$$(2) \dot{\epsilon}_{qps} = C_2 \frac{\rho_f \sigma}{\rho_s d^3} \frac{VcD_w}{RT}$$

where: C_2 is a shape constant; ρ_f and ρ_s are the fluid and solid densities (Kg m^{-3}), respectively; d is the grain size (μm); V is the molar volume ($\mu\text{m}^3 \text{mol}^{-1}$); c is the solubility of the solid in the fluid phase (molar fraction); D_w is the diffusivity of the solid in the grain-boundary fluid film ($\mu\text{m}^2 \text{s}^{-1}$). For feldspar, the flow laws of Rybacki et al. (2006) have been used to calculate the contribution of dislocation and diffusion creep:

$$(3) \dot{\epsilon} = A_f f_h \frac{\sigma^n}{d^m} e^{\left(-\frac{Q_f + pV^{act}}{RT}\right)}$$

where: A_f is the pre-exponential factor for feldspar ($\text{MPa}^{-n} \mu\text{m}^m \text{s}^{-1}$); d is the grain size (μm); m is the grain-size exponent ($m=3$ for diffusion creep; $m=0$ for dislocation creep); p is the confining pressure (MPa); V^{act} is the activation volume ($\text{m}^3 \text{mol}^{-1}$). Flow law parameters are listed in Table 1. The flow laws for poly-mineralic aggregates (e.g. sheared myrmekite and mica-free granitoid) have been calculated following the approach of Dimanov and Dresen (2005) and Platt (2015). Details on the derivation of the deformation mechanism maps and on the calculation of the flow laws are given in the online supplementary material.

The flow laws and flow law parameters were estimated for the pressure-temperature conditions of mylonitization of the Rieserferner (450 °C and 0.35GPa; Ceccato, 2018). At these conditions, the calculated water fugacity is $f_h = 97 \text{ MPa}$ (Pitzer and Sterner, 1994). Fluid density, Qtz solubility and diffusivity in the thin-film (grain boundary) fluid has been calculated following Fournier and Potter (1982) and Burnham et al. (1969). The flow law parameters defined for An_{100} and An_{60} by Rybacki and Dresen (2004) have been adopted for our calculations to simulate different compositions of “granitoid” and myrmekitic feldspars. These are “wet” flow law parameters that have been derived experimentally from deformation of fine grained aggregates of An_{100} and An_{60} containing 0.004 wt% and 0.3 wt% of water, respectively. In our calculations, all the Kfs has been considered as Plg, given the lack of flow law parameters for Kfs (see discussion in Platt, 2015; Viegas et al., 2016). Our calculation includes the contribution of GBS to the bulk strain rate of the feldspar aggregate, which is considered in the flow law parameters adopted here (see discussions in Xiao et al., 2002; Rybacki and Dresen, 2004).

7.3.1. Calculated rheology and strain partitioning in the Rieserferner mylonites

The grain-size vs. differential stress and differential stress vs. strain rate diagrams in Fig. 9 suggest the occurrence of different rheological behaviours that can be interpreted in terms of strain partitioning between aggregates with different “compositions”. The results indicate that the three considered types

of aggregates can be ranked, from the strongest to the weakest, as follows: (i) Qtz-feldspar “granitoid” aggregate; (ii) monomineralic Qtz aggregates (grain sizes of 4-10-20-100 μm); (iii) sheared myrmekite. This ranking is validated by several field and microstructural observations, which highlight the strain localization capability of monomineralic Qtz layers (i.e. Qtz veins) and two-phase
5 microstructural domains (i.e. sheared myrmekite) in granitoid rocks (Pennacchioni, 2005; Pennacchioni and Mancktelow, 2007; Menegon and Pennacchioni, 2010; Pennacchioni and Zucchi, 2013; Pennacchioni et al., 2010; Ceccato et al., 2017). The results of rheological calculation of Plg + Qtz aggregates deforming via diffusion creep (sheared myrmekite) are consistent and comparable with some of the experimental results of Xiao et al., (2002) extrapolated to natural geological conditions
10 (Fig. 9c). The experimental data that best fit our estimated rheological curve are those obtained from triaxial deformation experiments of synthetic very fine-grained wet aggregate of 80 vol% An₁₀₀ Plg (6 μm) + 20 vol% Qtz (10 μm).

Our results show that in the Rieserferner mylonites an effective strength contrast between mono- and poly-mineralic aggregates occurs as a consequence of the different deformation mechanisms. To
15 quantify the effective strength contrast between the modelled compositions, we consider two end-member conditions: constant stress and constant strain-rate. Assuming that the differential stress of 40-70 MPa, estimated from the finer grain size of Qtz (20-35 μm), is representative of the bulk flow stress of the mylonite, the Qtz aggregates deforming by dislocation creep (Fig. 9a) would flow at a strain rate of 10^{-11} - 10^{-13} s⁻¹ whereas sheared myrmekite deforming via diffusion creep would flow at
20 strain rates faster than 10^{-12} s⁻¹, depending on the actual grain size of the aggregate (red transparent area in Fig. 9b). For the grain size range of sheared myrmekite (4-7 μm), the observed strain rates are always faster than 10^{-11} s⁻¹, and for the above defined differential stress range the calculated strain rate is on the order of 10^{-9} s⁻¹ (intersection between red transparent area and black box in Fig. 9b). Therefore, assuming constant differential stress conditions, a strain-rate partitioning of 2-4 orders of
25 magnitude is expected between monomineralic Qtz and sheared myrmekite (similarly to Behrmann and Mainprice, 1987). Such strain-rate partitioning could also explain the observed decrease in Qtz grain size from the core of monomineralic layers toward neighbouring sheared myrmekite (Fig. 4).

Assuming constant strain rate conditions of 10^{-11} - 10^{-12} s⁻¹, the differential stress calculated for sheared myrmekite deforming via diffusion creep is <45 MPa. Under the constant strain rate assumption, the
30 strength contrast between monomineralic Qtz and sheared myrmekite is not quantifiable; however, the sheared myrmekite are always weaker than monomineralic Qtz deforming via dislocation creep. Strain

rates on the order of 10^{-11} - 10^{-13} s⁻¹ would require grain sizes in the range of 10-100 μm in the sheared myrmekite deforming by diffusion creep only (grey shaded areas in Fig. 9b).

7.3.2. The effect of myrmekite reaction

Figure 9d shows the different curves describing the rheological behaviour of a simplified granitoid rock where Kfs is progressively replaced, up to 20 vol%, by sheared myrmekite. The flow behaviour of the derived granitoid mylonite is represented by the grey curves, and is linear viscous for most of the investigated conditions. The complete consumption of Kfs results in 3-4 orders of magnitude increase of strain rate, consistent with experimental observations (Xiao et al., 2002). A similar increase in strain rate is already observed for a reaction progress factor of $\chi = 0.25$, i.e. for a 5 vol% of sheared myrmekite in the total rock volume. These results can be compared to the different degree of myrmekite substitution observed along the strain gradient in the shear zone and also justify the progressive increase in strain toward the ultramylonite with increasing myrmekite substitution (Fig. 2), suggesting positive feedback between strain-induced myrmekite formation and strain accommodation. Dissolution-precipitation creep of Kfs and associated GSS creep in Kfs + Plg + Qtz aggregates have been already described by Behrmann and Mainprice (1987) as an efficient strain accommodation and weakening mechanism in Qtz-feldspar mylonites. In the Rieserferner mylonites, GSS creep of Kfs seems to be dominant in protomylonite, but its role decreases with increasing myrmekite substitution (Fig. 2). The positive correlation between accommodated strain and myrmekite substitution suggests that GSS creep processes in Kfs are however not capable of accommodating strain at rates comparable to those produced by GSS creep in sheared myrmekite.

The effect of myrmekite development in rheological weakening might be overestimated by our calculation, for two main reasons: (i) other weakening mechanisms, that are not considered in our simplified model of granitoid (such as feldspar GSS creep, Bt deformation), may have concurred to deformation; and (ii) at low strain, myrmekite aggregates were initially non interconnected pockets (e.g. Handy, 1994). Strain weakening associated with myrmekite is inferred to become relevant as, with increasing strain and volume fraction of sheared myrmekite, the initially isolate myrmekite are sheared and coalesced into an interconnected network. In the Rieserferner sheared granodiorites an interconnected framework of sheared myrmekite is established in presence of 5 to 7 vol% of myrmekite and is well developed at 10-15 vol% (Fig. 2). Therefore, mylonites containing up to 15 vol% of sheared myrmekite ideally underwent deformation at strain rates of 10^{-10} - 10^{-11} s⁻¹ and at differential stresses in the range between 14 and 70 MPa. These mylonites were synkinematic to mylonitic Qtz veins

described in Ceccato et al. (2017), for which Qtz paleopiezometry retrieved comparable strain rates of 10^{-11} s^{-1} for 117 MPa differential stress.

8. Conclusions

Metamorphic reactions contributed importantly to strain weakening within the Rieserferner granitoid mylonites. A primary grain size reduction mechanism was related to the development of myrmekite evolving, with increasing strain, to weak aggregates of Qtz and Plg. Topotactic replacement has been inferred from the coincidence between myrmekitic Plg and parent Kfs grain crystal lattices in pristine myrmekite. Transition from pristine myrmekite to fine-grained sheared myrmekite involved microfracturing, annealing and shearing of the resulting granoblastic aggregate. Sheared myrmekite consists of fine grained Plg + Qtz aggregates (7 μm and 4 μm in grain size, respectively) that show anticlustered spatial distribution and well-defined shape preferred orientation; Qtz usually occurs at triple- and quadruple-junction between Plg grains. Both Plg and Qtz show weak CPOs and almost uniform misorientation angle distributions. The microstructures of sheared myrmekite suggest that different deformation mechanisms occurred in Plg and Qtz: Plg deformed mainly by GSS creep, whereas dissolution-precipitation and nucleation processes were dominant in Qtz. Myrmekite formation promoted also phase mixing, as the pristine myrmekite microstructure predisposed the development of an “anticlustered” spatial distribution of phases in the recrystallized aggregate. Strong grain size reduction and the nucleation of Plg + Qtz polymineralic aggregates led to a switch in the dominant deformation mechanisms, activating GSS creep processes and triggered phase mixing. GSS processes and phase mixing inhibited grain growth and stabilized grain size, hindering the efficiency of dynamic recrystallization processes and self-sustaining the activity of GSS processes. Therefore, the formation of myrmekite led to the activation of self-sustaining weakening processes.

Results of rheological calculations show that, at the conditions of Rieserferner mylonitization, sheared myrmekite are several orders of magnitude weaker than both pure Qtz layers and ideal granitoid rock deforming via dislocation creep. Strain-rate partitioning is therefore expected to occur between sheared myrmekite and monomineralic Qtz layers, and the occurrence of ca. 5 vol% of myrmekite could lead to an increase of 3-4 orders of magnitude in strain rate. However, the effective role of myrmekite in rock weakening depends on the evolution of the rock microstructure. Effective weakening requires interconnection of sheared myrmekite layers, which occurs after the development of 10-15 vol% of myrmekite.

This work highlights the importance of metamorphic reactions as grain size reduction mechanisms in

feldspar, and their role in localization of ductile deformation via the activation of grain size sensitive creep. The microstructural results and the rheological calculation presented here will be useful for further development of detailed rheological models of feldspar-rich rocks at mid-crustal conditions.

Code availability

- 5 The MATLAB script used for rheological calculation is available on request from the first author.

Data availability

Supplementary data are available in Supplementary Online Material (SOM).

Appendix A: Methods

A.1 EBSD sample preparation and data processing

- 10 The thin section was SYTON-polished for ca. 3 hours and carbon coated. All data have been processed and analysed using CHANNEL5 software of HKL Technology, Oxford Instruments. Noise reduction was applied following Bestmann and Prior (2003). Local mis-indexing between Plg and Kfs was resolved by nullifying the subset of selected grains with area $<1\mu\text{m}^2$ in each map. Dauphiné twins smaller than $0.5\ \mu\text{m}$ have been interpreted as an error from mis-indexing and were replaced by the
15 average orientation of the neighbouring pixels. The indexed phases and relative symmetry group used for the indexing are: quartz – Trigonal -3m; plagioclase (anorthite) – Triclinic -1; orthoclase – Monoclinic 2/m. Critical misorientation for the distinction between low- and high-angle boundaries have been chosen at 10° . Qtz grain boundaries with $60^\circ\pm 5^\circ$ of misorientation were disregarded from grain detection procedure, to avoid any contribution from Dauphiné twinning. Plg grain boundaries
20 with $180^\circ\pm 5^\circ$ of misorientation around [010] were disregarded from grain detection procedure, to avoid any contribution from Albite twinning. The pole figures (one-point-per-grain, where not differently specified) are plotted as equal area, lower hemisphere projections oriented with the general shear zone kinematics reference system (X = stretching lineation; Z = pole to general shear plane/vein boundary); whereas the misorientation axis distributions in sample coordinates are plotted as equal
25 area, upper hemisphere projections. The inverse pole figures for misorientation axis distribution in crystal coordinates are upper hemisphere projections. Contoured projections have constant contouring parameters (Halfwidth: 10°). Contouring lines are given only for the 0.5-10 m.u.d. (multiple of uniform distributions) range.

A.2 Grain size analysis

Grain sizes were obtained from the grain detection routine of the HKL Channel5 Tango software. The grain size was calculated as diameter of the circle with an equivalent area. The minimum cut-off area was set to $1 \mu\text{m}^2$ which means that only grains of a size ≥ 4 or ≥ 9 pixels (depending on the map acquisition step-size) were considered. Grain size data were represented as area-weighted distributions by plotting frequency against the square-root grain-size-equivalent grain diameters (as in Herwegh and Berger, 2004; Berger et al., 2011). The grain size distribution approaches a Gaussian distribution when plotted in this way, allowing a good estimate of the mean grain size. The geometric mean grain size (red thick line in grain size distribution diagrams) was obtained graphically as the maximum frequency grain size of the distribution curve. The distribution curve (blue line in grain size distribution diagrams) was obtained interpolating distribution data with a 6th degree polynomial equation in Excel-MS Office. Relative frequencies are normalized to 1.

A.3 Image analysis

Image analysis of grain shape was performed on both SEM-BSE images and phase maps obtained from EBSD. Quantification of phase amount (vol%) was performed through segmentation of SEM-BSE images of a whole thin section collected at the Electron Microscopy Centre of the University of Plymouth. Image processing and thresholding was done with the ImageJ software, and further processing together with manual correction were applied to improve data quality and to ensure the correspondence of greyscale ranges with specific mineral phases. Grain boundary images and phase distribution images were obtained directly from EBSD phase maps and grain boundary maps elaborated by Channel5 (HKL technology). Before the analysis with ImageJ software, images were manually corrected in order to exclude mis-indexing and non-indexed orientation pixels. Grain boundaries and phase amount have been quantified by pixel counting.

Author contributions

AC, LM and GP developed the initial idea of the study and performed initial exploratory SEM study. GP collected the samples of Rieserferner mylonites. LM acquired EBSD data. AC performed EBSD data processing and analysis, and the rheological calculations. LFGM performed cathodoluminescence analysis. AC prepared the figures and the manuscript with contributions from all the co-authors.

Competing interests

The authors declare that they have no conflict of interest.

Acknowledgements

Elena A. Miranda and an anonymous reviewer are warmly thanked for their comments and reviews. Simone Papa, Francesco Giuntoli, Luca Pellegrino are thanked for fruitful discussions. Andrea Risplendente is thanked for his help during EMPA data collection at the Università degli Studi di
5 Milano. The staff at University of Plymouth Electron Microscopy Centre is thanked for the assistance during EBSD data acquisition. Luca Menegon acknowledges the financial support from a FP7 Marie Curie Career Integration Grant (grant agreement PCIG13-GA-2013-618289). Financial support from the University of Padova (“Progetto di Ateneo” CPDA140255) and from the Foundation “Ing. Aldo Gini” is acknowledged.

References

- Abart, R., Heuser, D., and Habler, G.: Mechanisms of myrmekite formation: case study from the Weinsberg granite, Moldanubian zone, Upper Austria. *Contributions to Mineralogy and Petrology* 5 168, 1074, 2014.
- Becke, F.: Über myrmekite. *Mineralogie und Pétrographie Mitteilungen* 27, 377-390, 1908.
- Behrmann, J.H. and Mainprice, D.: Deformation mechanisms in a high-temperature quartz-feldspar mylonite: evidence for superplastic flow in the lower continental crust. *Tectonophysics* 140, 297-305, 1987.
- 10 Bellieni, G.: Caratteri geochimici del massiccio granodioritico tonalitico delle Vedrette di Ries (Rieserferner) - Alto Adige Orientale. *Rendiconti della Società Italiana di Mineralogia e Petrologia* 34, 527-548, 1978.
- Bestmann, M. and Prior, D.J.: Intragranular dynamic recrystallization in naturally deformed calcite marble: diffusion accommodated grain boundary sliding as a result of subgrain rotation 15 recrystallization. *Journal of Structural Geology* 25, 1597-1613, 2003.
- Bestmann, M. and Pennacchioni, G.: Ti distribution in quartz across a heterogeneous shear zone within a granodiorite: The effect of deformation mechanism and strain on Ti resetting. *Lithos*, 227, 37-56, 2015.
- Boullier, A. M., and Gueguen, Y.: SP-mylonites: origin of some mylonites by superplastic 20 flow. *Contributions to Mineralogy and Petrology*, 50, 93-104, 1975.
- Burnham, C.W., Holloway, J.R., and Davis, N.F.: *Thermodynamic Properties of Water to 1,000 °C and 10,000 Bars*. Geological Society of America, 132, <https://doi.org/10.1130/SPE132> , 1969.
- Ceccato, A., 2018. Structural evolution of Periadriatic plutons and its implications on solid-state deformation of granitoid rocks. Università degli Studi di Padova. PhD Thesis, pp. 250.
- 25 Ceccato, A., Pennacchioni, G., Menegon, L., and Bestmann, M.: Crystallographic control and texture inheritance during mylonitization of coarse grained quartz veins. *Lithos* 290-291, 210-227, doi:10.1016/j.lithos.2017.08.005 , 2017.
- Ceccato, A. and Pennacchioni, G.: Structural evolution of the Rieserferner Pluton in the framework of the Tertiary tectonics of the Eastern Alps. *Journal of Structural Geology*. 2018. 30 <https://doi.org/10.1016/j.jsg.2018.08.004>

- Cesare, B., Marchesi, C., and Connolly, J.A.D.: Growth of myrmekite coronas by contact metamorphism of granitic mylonites in the aureole of Cima di Vila, Eastern Alps, Italy. *Journal of Metamorphic Geology* 20, 203-213, 2002.
- Cesare, B., Mazzoli, C., Sassi, R., Spiess, R., and Sassi, F.P.: Beauty and complexity of metamorphism: case studies from the frontal part of the Adria microplate. *Rendiconti Lincei* 21, 73-94, 2010.
- Ciancaleoni, L., and Marquer, D.: Syn-extension leucogranite deformation during convergence in the Eastern Central Alps: example of the Novate intrusion. *Terra Nova* 18, 170-180, 2006.
- Cross, A. J., Prior, D. J., Stipp, M., and Kidder, S.: The recrystallized grain size piezometer for quartz: An EBSD-based calibration. *Geophysical Research Letters*, 44, 6667-6674, 2017.
- Czaplińska, D., Piazzolo, S., and Zibra, I.: The influence of phase and grain size distribution on the dynamics of strain localization in polymineralic rocks. *Journal of Structural Geology* 72, 15-32 2015.
- De Toni, G. B., Bitencourt, M. F., and Nardi, L. V. S.: Strain partitioning into dry and wet zones and the formation of Ca-rich myrmekite in syntectonic syenites: A case for melt-assisted dissolution-replacement creep under granulite facies conditions. *Journal of Structural Geology*, 91, 88-101, 2016.
- Dégi, J., Abart, R., Török, K., Bali, E., Wirth, R., and Rhede, D.: Symplectite formation during decompression induced garnet breakdown in lower crustal mafic granulite xenoliths: mechanisms and rates. *Contributions to Mineralogy and Petrology*, 159, 293-314, 2010.
- Dell'Angelo, L.N. and Tullis, J.: Textural and mechanical evolution with progressive strain in experimentally deformed aplite. *Tectonophysics* 256, 57-82, 1996.
- Den Brok, S.W.J.: Effect of microcracking on pressure-solution strain rate: The Gratz grain-boundary model. *Geology* 26, 915-918, 1998.
- Dimanov, A., and Dresen, G.: Rheology of synthetic anorthite-diopside aggregates: Implications for ductile shear zones. *Journal of Geophysical Research: Solid Earth* 110. <https://doi.org/10.1029/2004JB003431> , 2005.
- Farver, J. R. and Yund, R. A.: Interphase boundary diffusion of oxygen and potassium in K-feldspar/quartz aggregates. *Geochimica et Cosmochimica Acta*, 59, 3697-3705, 1995
- Fliervoet, T.F., White, S.H., and Drury, M.R.: Evidence for dominant grain-boundary sliding deformation in greenschist-and amphibolite-grade polymineralic ultramylonites from the Redbank Deformed Zone, Central Australia. *Journal of Structural Geology* 19, 1495-1520, 1997.
- Fournier, R.O. and Potter II, R.W.: An equation correlating the solubility of quartz in water from 25 to 900 °C at pressures up to 10,000 bars. *Geochimica et Cosmochimica Acta* 46, 1969-1973, 1982.

- Fusseis, F., Regenauer-Lieb, K., Liu, J., Hough, R.M., and De Carlo, F.: Creep cavitation can establish a dynamic granular fluid pump in ductile shear zones. *Nature* 459, 974, 2009.
- Götze, J., Habermann, D., Neuser, R. D., and Richter, D. K.: High-resolution spectrometric analysis of rare earth elements-activated cathodoluminescence in feldspar minerals. *Chemical Geology*, 153, 81-91, 1999.
- Gueydan, F., Leroy, Y. M., Jolivet, L., Agard, P.: Analysis of continental midcrustal strain localization induced by microfracturing and reaction-softening. *Journal of Geophysical Research: Solid Earth*, 108(B2), 2003.
- Handy, M.R.: The solid-state flow of polymineralic rocks. *Journal of Geophysical Research: Solid Earth* 95, 8647-8661, 1990.
- Handy, M.R.: Flow laws for rocks containing two non-linear viscous phases: a phenomenological approach. *Journal of Structural Geology* 16, 287-301, 1994.
- Herwegh, M. and Berger, A.: Deformation mechanisms in second-phase affected microstructures and their energy balance. *Journal of Structural Geology* 26, 1483-1498, 2004.
- Herwegh, M., Linckens, J., Ebert, A., Berger, A., and Brodhag, S. H.: The role of second phases for controlling microstructural evolution in polymineralic rocks: A review. *Journal of Structural Geology* 33, 1728-1750, 2011.
- Hiraga, T., Miyazaki, T., Yoshida, H., and Zimmerman, M.E.: Comparison of microstructures in superplastically deformed synthetic materials and natural mylonites: Mineral aggregation via grain boundary sliding. *Geology* 41, 959-962, 2013
- Hirth, G., Teyssier, C., and Dunlap, J.W.: An evaluation of quartzite flow laws based on comparisons between experimentally and naturally deformed rocks. *International Journal of Earth Sciences* 90, 77-87, 2001.
- Hopson, R.F. and Ramseyer, K.: Cathodoluminescence microscopy of myrmekite. *Geology* 18, 336-339, 1990.
- Jiang, Z., Prior, D.J., and Wheeler, J.: Albite crystallographic preferred orientation and grain misorientation distribution in a low-grade mylonite: implications for granular flow. *Journal of Structural Geology* 22, 1663-1674, 2000.
- Johnson, S.E., Marsh, J.H., and Vernon, R.H.: From tonalite to mylonite: coupled mechanical and chemical processes in foliation development and strain localization. *Journal of Virtual Explorer* 30, 2008.
- Kilian, R., Heilbronner, R., and Stünitz, H.: Quartz grain size reduction in a granitoid rock and the transition from dislocation to diffusion creep. *Journal of Structural Geology* 33, 1265-1284, 2011.
- Kretz, R.: Symbols for rock-forming minerals. *American mineralogist*, 68, 277-279, 1983.

- Kruse, R. and Stünitz, H.: Deformation mechanisms and phase distribution in mafic high-temperature mylonites from the Jotun Nappe, southern Norway. *Tectonophysics* 303, 223-249, 1999.
- Kruse, R., Stünitz, H., and Kunze, K.: Dynamic recrystallization processes in plagioclase porphyroclasts. *Journal of Structural Geology* 23, 1781-1802, 2001.
- 5 Lapworth, T., Wheeler, J., and Prior, D.J.: The deformation of plagioclase investigated using electron backscatter diffraction crystallographic preferred orientation data. *Journal of Structural Geology* 24, 387-399, 2002.
- LaTour, T. E. and Barnett, R. L.: Mineralogical changes accompanying mylonitization in the Bitterroot dome of the Idaho batholith: Implications for timing of deformation. *Geological Society of America*
- 10 *Bulletin*, 98, 356-363, 1987.
- McCaffrey, K. J.: Magmatic and solid state deformation partitioning in the Ox Mountains Granodiorite. *Geological Magazine*, 131, 639-652, 1994.
- Menegon, L., Pennacchioni, G., and Stünitz, H.: Nucleation and growth of myrmekite during ductile shear deformation in metagranites. *Journal of Metamorphic Geology* 24, 553-568, 2006.
- 15 Menegon, L., Pennacchioni, G., and Spiess, R.: Dissolution-precipitation creep of K-feldspar in mid-crustal granite mylonites. *Journal of Structural Geology*, 30, 565-579, 2008.
- Menegon, L. and Pennacchioni, G.: Local shear zone pattern and bulk deformation in the Gran Paradiso metagranite (NW Italian Alps). *International Journal of Earth Sciences* 99, 1805-1825, doi:10.1007/s00531-009-0485-6 , 2010.
- 20 Menegon, L., Stünitz, H., Nasipuri, P., Heilbronner, R., and Svahnberg, H.: Transition from fracturing to viscous flow in granulite facies perthitic feldspar (Lofoten, Norway). *Journal of Structural Geology* 48, 95-112, 2013.
- Menegon, L., Füsseis, F., Stünitz, H., and Xiao, X.: Creep cavitation bands control porosity and fluid flow in lower crustal shear zones. *Geology* 43, 227-230, 2015.
- 25 Michibayashi, K.: The role of intragranular fracturing on grain size reduction in feldspar during mylonitization. *Journal of Structural Geology*, 18, 17-25, 1996.
- Miranda, E.A., Hirth, G., and John, B.E.: Microstructural evidence for the transition from dislocation creep to dislocation-accommodated grain boundary sliding in naturally deformed plagioclase. *Journal of Structural Geology* 92, 30-45, 2016.
- 30 O'Hara, K. D., Sharp, Z. D., Moecher, D. P., Jenkin, G. T.: The effect of deformation on oxygen isotope exchange in quartz and feldspar and the significance of isotopic temperatures in mylonites. *The Journal of Geology*, 105, 193-204, 1997.
- Odashima, N., Morishita, T., Ozawa, K., Nagahara, H., Tsuchiyama, A., and Nagashima, R.: Formation and deformation mechanisms of pyroxene-spinel symplectite in an ascending mantle,

- the Horoman peridotite complex, Japan: An EBSD (electron backscatter diffraction) study. *Journal of Mineralogical and Petrological Sciences*, 103, 1-15, 2007.
- Okudaira, T., and Shigematsu, N.: Estimates of stress and strain rate in mylonites based on the boundary between the fields of grain-size sensitive and insensitive creep. *Journal of Geophysical Research: Solid Earth*, 117(B3), 2012.
- Pennacchioni, G.: Control of the geometry of precursor brittle structures on the type of ductile shear zone in the Adamello tonalites, Southern Alps (Italy). *Journal of Structural Geology* 27, 627-644, 2005.
- Pennacchioni, G., Di Toro, G., Brack, P., Menegon, L., and Villa, I.M.: Brittle–ductile–brittle deformation during cooling of tonalite (Adamello, Southern Italian Alps). *Tectonophysics* 427, 171-197, 2006.
- Pennacchioni, G., and Mancktelow, N.S.: Nucleation and initial growth of a shear zone network within compositionally and structurally heterogeneous granitoids under amphibolite facies conditions. *Journal of Structural Geology* 29, 1757-1780, 2007.
- Pennacchioni, G., and Mancktelow, N.S.: Small-scale ductile shear zones: neither extending, nor thickening, nor narrowing. *Earth-Science Reviews* 184, 1-12, 2018
- Pennacchioni, G. and Mancktelow, N.S.: Small-scale ductile shear zones: neither extending, nor thickening, nor narrowing. *Earth-Science Reviews*, doi:10.1016/j.earscirev.2018.06.004 , 2018.
- Pennacchioni, G. and Zucchi, E.: High temperature fracturing and ductile deformation during cooling of a pluton: The Lake Edison granodiorite (Sierra Nevada batholith, California). *Journal of Structural Geology* 50, 54-81, 2013.
- Phillips, E. R.: On polygenetic myrmekite. *Geological Magazine*, 117, 29-36, 1980.
- Pitzer, K. S. and Sterner, S.M.: Equations of state valid continuously from zero to extreme pressures for H₂O and CO₂. *The Journal of Chemical Physics* 101, 3111-3116, 1994.
- Platt, J.P.: Rheology of two-phase systems: A microphysical and observational approach. *Journal of Structural Geology* 77, 213-227, 2015.
- Ramseyer, K., AlDahan, A. A., Collini, B., and Landström, O.: Petrological modifications in granitic rocks from the Siljan impact structure: evidence from cathodoluminescence. *Tectonophysics*, 216, 195-204, 1992.
- Ree, J.H., Kim, H.S., Han, R., and Jung, H.: Grain-size reduction of feldspars by fracturing and neocrystallization in a low-grade granitic mylonite and its rheological effect. *Tectonophysics* 407, 227-237, 2005.
- Rybacki, E. and Dresen, G.: Deformation mechanism maps for feldspar rocks. *Tectonophysics* 382, 173-187, 2004.

- Rybacki, E., Gottschalk, M., Wirth, R., and Dresen, G.: Influence of water fugacity and activation volume on the flow properties of fine-grained anorthite aggregates. *Journal of Geophysical Research: Solid Earth* 111. <https://doi.org/10.1029/2005JB003663> , 2006.
- Romer, R.L. and Siegesmund, S.: Why allanite may swindle about its true age. *Contributions to Mineralogy and Petrology* 146, 297-307, 2003.
- 5 Segall, P. and Simpson, C.: Nucleation of ductile shear zones on dilatant fractures. *Geology*, 14, 56-59, 1986.
- Shimamoto, T., Kanaori, Y., Asai, K. I.: Cathodoluminescence observations on low-temperature mylonites: potential for detection of solution-precipitation microstructures. *Journal of Structural*
- 10 *Geology*, 13, 967-973, 1991.
- Simpson, C. and Wirth, R.P.: Evidence for deformation-induced K-feldspar replacement by myrmekite. *Journal of Metamorphic Geology* 7, 261-275, 1989.
- Słaby, E., Götze, J., Wörner, G., Simon, K., Wrzalik, R., and Śmigielski, M.: K-feldspar phenocrysts in microgranular magmatic enclaves: a cathodoluminescence and geochemical study of crystal
- 15 growth as a marker of magma mingling dynamics. *Lithos*, 105, 85-97, 2008.
- Słaby, E., Domonik, A., Śmigielski, M., Majzner, K., Motuza, G., Götze, J., Rydelek, P.: Protomylonite evolution potentially revealed by the 3D depiction and fractal analysis of chemical data from a feldspar. *Contributions to Mineralogy and Petrology*, 167, 995, 2014.
- Stel, H. and Breedveld, M.: Crystallographic orientation patterns of myrmekitic quartz: a fabric
- 20 memory in quartz ribbon-bearing gneisses. *Journal of Structural Geology* 12, 19-28, 1990.
- Stipp, M., Stünitz, H., Heilbronner, R., Schmid, S.M.: The eastern Tonale fault zone: a 'natural laboratory' for crystal plastic deformation of quartz over a temperature range from 250 to 700 °C. *Journal of Structural Geology* 24, 1861-1884, 2002.
- Stipp, M. and Tullis, J.: The recrystallized grain size piezometer for quartz. *Geophysical Research*
- 25 *Letters*, 30, 2003.
- Stipp, M., Tullis, J., Scherwath, M., and Behrmann, J. H. A new perspective on paleopiezometry: Dynamically recrystallized grain size distributions indicate mechanism changes. *Geology*, 38, 759-762, 2010.
- Stünitz, H. and Fitz Gerald, J.F.: Deformation of granitoids at low metamorphic grade. II: Granular
- 30 flow in albite-rich mylonites. *Tectonophysics* 221, 299-324, 1993.
- Stünitz, H., and Tullis, J.: Weakening and strain localization produced by syn-deformational reaction of plagioclase. *International Journal of Earth Sciences*, 90(1), 136-148, 2001.

- Tsurumi, J., Hosonuma, H., and Kanagawa, K.: Strain localization due to a positive feedback of deformation and myrmekite-forming reaction in granite and aplite mylonites along the Hatagawa Shear Zone of NE Japan. *Journal of Structural Geology* 25, 557-574, 2003.
- Tullis, J. and Yund, R. A.: Transition from cataclastic flow to dislocation creep of feldspar: Mechanisms and microstructures. *Geology*, 15, 606-609, 1987.
- Tullis, J. and Yund, R. A.: The brittle-ductile transition in feldspar aggregates: An experimental study. *International Geophysics* (Vol. 51, pp. 89-117). Academic press, 1992.
- Vernon, R.H.: Questions about myrmekite in deformed rocks. *Journal of Structural Geology* 13, 979-985, 1991.
- 10 Viegas, G., Menegon, L., and Archanjo, C.: Brittle grain-size reduction of feldspar, phase mixing and strain localization in granitoids at mid-crustal conditions (Pernambuco shear zone, NE Brazil). *Solid Earth* 7, 375-396, 2016.
- Wheeler, J., Prior, D., Jiang, Z., Spiess, R., and Trimby, P.: The petrological significance of misorientations between grains. *Contributions to Mineralogy and Petrology* 141, 109-124, 2001.
- 15 White, S.: Geological significance of recovery and recrystallization processes in quartz. *Tectonophysics* 39, 143-170, 1977.
- Wirth, R. and Voll, G.: Cellular intergrowth between quartz and sodium-rich plagioclase (myrmekite)—an analogue of discontinuous precipitation in metal alloys. *Journal of Materials Science* 22, 1913-1918, 1987.
- 20 Xiao, X., Wirth, R., and Dresen, G.: Diffusion creep of anorthite-quartz aggregates. *Journal of Geophysical Research: Solid Earth* 107(B11), 2002.

Figure and Tables Captions

Table 1. Parameters adopted in the rheological calculations. (a) List of the general parameters adopted in the rheological calculations. (b) Values of flow law parameters adopted in the rheological calculations according to mineral phase and deformation mechanism.

5 **Figure 1.** Microstructures of Rieserferner granodiorite mylonites. (a) Microphotograph (crossed polarizers) showing the alternating layers of recrystallized Qtz, of recrystallized Bt + Plg + Qtz, and of Plg + Qtz. White arrows indicate layers of recrystallized Qtz (upper) and Bt (lower). (b) SEM-BSE image of the area shown in (a). (c) SEM-BSE image of a pristine myrmekite (Myrm) replacing Kfs. (d) SEM-BSE image of the Kfs + Bt tails in strain shadows between two Plg porphyroclasts. Kfs in
10 the strain shadows is in turn replaced by myrmekite (white arrows). (e) SEM-BSE image of a Kfs porphyroclast and of sheared myrmekite. Pristine myrmekite developed on Kfs boundaries parallel to the mylonitic foliation are sheared to form Plg + Qtz aggregates (sheared myrmekite). The white polygon encloses Kfs neoblasts in strain shadows and sheared myrmekite. (f) CL image of (e). Note the alteration of the CL signal in Qtz after the EBSD scan (area delimited by white dashed line). (g)
15 Kfs and sheared myrmekite aggregate (particular of the EBSD map of Fig. 3). (h) CL image of (g).

Figure 2. Phase distribution and abundance across a strain gradient in a granodiorite mylonite. (a) Mosaic of SEM-BSE images with the Kfs and the myrmekite + sheared myrmekite coloured in red and pale blue, respectively. The yellow rectangles indicate the location of the EBSD maps of Figs. 3, 4, 5 and SOM2. (b) Bar diagram showing the volume amount of Kfs (red bars) and myrmekite (pale
20 blue bars) across the microstructure: PM = protomylonite; M = mylonite; and UM = ultramylonite.

Figure 3. EBSD map and crystallographic orientation data of incipient myrmekite and parent Kfs. (a) EBSD-derived phase map. The area delimited by dashed polygons represents pristine myrmekite. Pole figures for: (b) Kfs grains on which pristine myrmekite nucleated; (c) Plg and (d) Qtz in pristine myrmekite.

25 **Figure 4.** EBSD map and crystallographic orientation data of pristine and sheared myrmekite of Fig. 1e. (a) EBSD phase map including areas (A, B, C, D) selected for grain size analysis and phase distribution analysis. (b) Pole figures for Qtz from the sheared myrmekite of Area B. Upper row: scattered data. Lower row: contoured data. (c) Misorientation axis distributions for Qtz in sample (upper row) and crystal (lower row) coordinate system. (d) Misorientation angle distribution for Qtz.
30 (e) Pole figures for Plg from sheared myrmekite of Area B. Upper row: scattered data. Lower row: contoured data. In this case, the [100] Plg pole figure is reported in upper hemisphere, where the

maximum has been observed. (f) Misorientation axis distributions for Plg in sample (upper row) and crystal (lower row) coordinate system. (g) Misorientation angle distribution for Plg. (h) Pole figures of the crystallographic orientation of Kfs porphyroclasts included in Areas C and E and respective tails. (i) Misorientation axis distributions in sample (upper row) and crystal (lower row) coordinate system for porphyroclasts and tails. (j) Pole figures of the crystallographic orientation of Kfs porphyroclast A and Kfs neoblasts in the strain shadow (Area D). (k) Misorientation axis distributions in sample (upper row) and crystal (lower row) coordinate system for Kfs neoblasts. (l) Grain size distribution for the Kfs neoblasts.

10 **Figure 5.** EBSD orientation data and mapping for pure Qtz layers. (a) Orientation map colour coded according to the inverse pole figure for Y-direction reported in the lower right corner. (b) Area-weighted grain size distribution for pure Qtz layer. (b) Pole figures for Qtz [c], <a> and {r} crystallographic elements. (c) Misorientation axis distributions in sample (upper row) and crystal (lower row) coordinate system. (d) Misorientation angle distribution for Qtz.

15

Figure 6. Image analysis of the phase spatial distribution in myrmekite. The diagram reports phase- and grain-boundary fractions in pristine- and sheared myrmekite. Continuous curves represent the theoretical probability of phase- and grain-boundary fraction as a function of Qtz content expected for a random distribution in a two-phase aggregate. The small maps on the left hand side report one of the analysed areas (Area C. Fig. 4), showing from the top to the bottom the phase map, the Plg grain boundaries, the Qtz grain boundaries, and the Plg-Qtz phase boundaries.

Figure 7. Area-weighted grain size distributions and SPO for Qtz. (a) Grain size distribution for Qtz in incipient myrmekite A in Fig. 4a. (b) Grain size distribution for Qtz in sheared myrmekite B in Fig. 4a. (c) Grain size distribution for Qtz in sheared myrmekite C in Fig. 4a. (d) Grain size distribution for Qtz in monomineralic layer in Fig. 4a. (e) Relative frequency distribution of grain aspect ratio for Qtz. (f) Rose diagram showing the orientation of major axis of Qtz grains, defining a weak SPO.

Figure 8. Area-weighted grain size distributions and SPO for Plg. (a) Grain size distribution for Plg in myrmekite of Fig. 3. (b) Grain size distribution for Plg in incipient myrmekite A in Fig. 4a. (c) Grain size distribution for Plg in sheared myrmekite B in Fig. 4a. (d) Relative frequency distribution of grain aspect ratio for Plg. (e) Rose diagram showing the orientation of major axis of Plg grains, defining a weak SPO.

30

Figure 9. Diagrams derived from the calculation of the rheological model explained in the text. Grain size vs. differential stress map with contoured strain rate curves calculated for: (a) Qtz, (b) 80% Plg (An₆₀) + 20% Qtz aggregates. (a) The piezometric curve from Stipp and Tullis (2003) (black curve) and Cross et al. (2017) (red curve) are reported. Red and black stars mark the differential stress/strain-rate conditions defined by the grain size observed in pure Qtz layers: (A) 35 μm; (B) 20 μm; (C) 10 μm (Ceccato et al., 2017). (b) A and B marked red polygons represent the differential stress range derived from piezometric calculations on pure Qtz layers (red and black stars along respective piezometric curves). The black dashed line represents the boundary between dislocation and diffusion creep dominated conditions. The black rectangle represents the grain size range (4-7 μm) observed in the sheared myrmekite. The grey semi-transparent polygon defines the field of possible grain-size and differential stress conditions for iso-strain-rate conditions defined from piezometric relations. (c) Log differential stress vs. Log strain rate diagram reporting the curve calculated for pure Qtz with different grain sizes, sheared myrmekite, ideal granitoid rock and the curves representing the rheology of pure feldspar aggregates. For comparison, one of the curve obtained from experimental data of Xiao et al., (2002) is reported (black dashed curve). Grey field represents the uncertainties on the experimentally defined rheological curve. (d) Log differential stress vs. Log strain rate diagram reporting the curve calculated for pure Qtz, sheared myrmekite and ideal granitoid rock and the curves representing the rheology of a granitoid (60% An₁₀₀ Plg+ 40% Qtz) with variable amount of sheared myrmekite (80% An₆₀ Plg + 20% Qtz). Maximum replacement is limited to 20% of initial feldspar (see text for explanation).

| Parameter | Description | Value | Units | Reference |
|------------------|-----------------------------------------------------------|--------------|------------------------|------------------|
| P | Pressure | 350 | MPa | 4 |
| T | Temperature | 723 | K | 4 |
| f_h | Water fugacity | 97 | MPa | 5 |
| R | Gas constant | 8.314 | $J K^{-1} mol^{-1}$ | |
| d | Grain size | | μm | |
| n | Stress exponent | | | 1,2 |
| m | Grain size exponent | | | 1,2 |
| A | Pre-exponential factor | | $MPa^n \mu m^m s^{-1}$ | 1,2 |
| Q | Activation energy | | J | 1,2 |
| ρ_f | Fluid density | 837.5 | $Kg m^{-3}$ | |
| ρ_s | Solid density | 2650 | $Kg m^{-3}$ | |
| C_2 | Shape constant | 44 | | 3 |
| V | Molar Volume of quartz | 22690000 | $\mu m^3 mol^{-1}$ | |
| c | Solubility of solid in the fluid phase | 0.0014 | molar fraction | 6 |
| D_w | Diffusivity of the solid in the grain-boundary fluid film | 1.604E-11 | $\mu m^2 s^{-1}$ | 3 |
| V^{act} | Activation volume | 0.00038 | $m^3 mol^{-1}$ | 7 |
| μ | Viscosity | | $MPa s^{-1}$ | a |

| Parameter | Dislocation creep | | | Diffusion Creep | | | b |
|------------------|--------------------------|-------------------|------------------|------------------------|-------------------|------------------|----------|
| | Quartz | Plagioclase | | Quartz | Plagioclase | | |
| Phase | Quartz | An ₁₀₀ | An ₆₀ | Quartz | An ₁₀₀ | An ₆₀ | |
| Composition | | An ₁₀₀ | An ₆₀ | | An ₁₀₀ | An ₆₀ | |
| n | 4 | 3 | 3 | 1 | 1 | 1 | |
| m | 0 | 0 | 0 | 3 | 3 | 3 | |
| A | 6.30957E-12 | 398.1 | 0.031 | | 50.1 | 12.6 | |
| Q | 135000 | 345000 | 235000 | 137000 | 159000 | 153000 | |
| Reference | 1 | 2 | 2 | 3 | 2 | 2 | |

References:

- (1) Hirth et al., 2001.
- (2) Rybacki and Dresen, 2004.
- (3) den Brok, 1998.
- (4) Ceccato, 2018.
- (5) Pitzer and Sterner, 1994.
- (6) Fourniery and Potter, 1982.
- (7) Rybacki et al., 2006.

Table 1

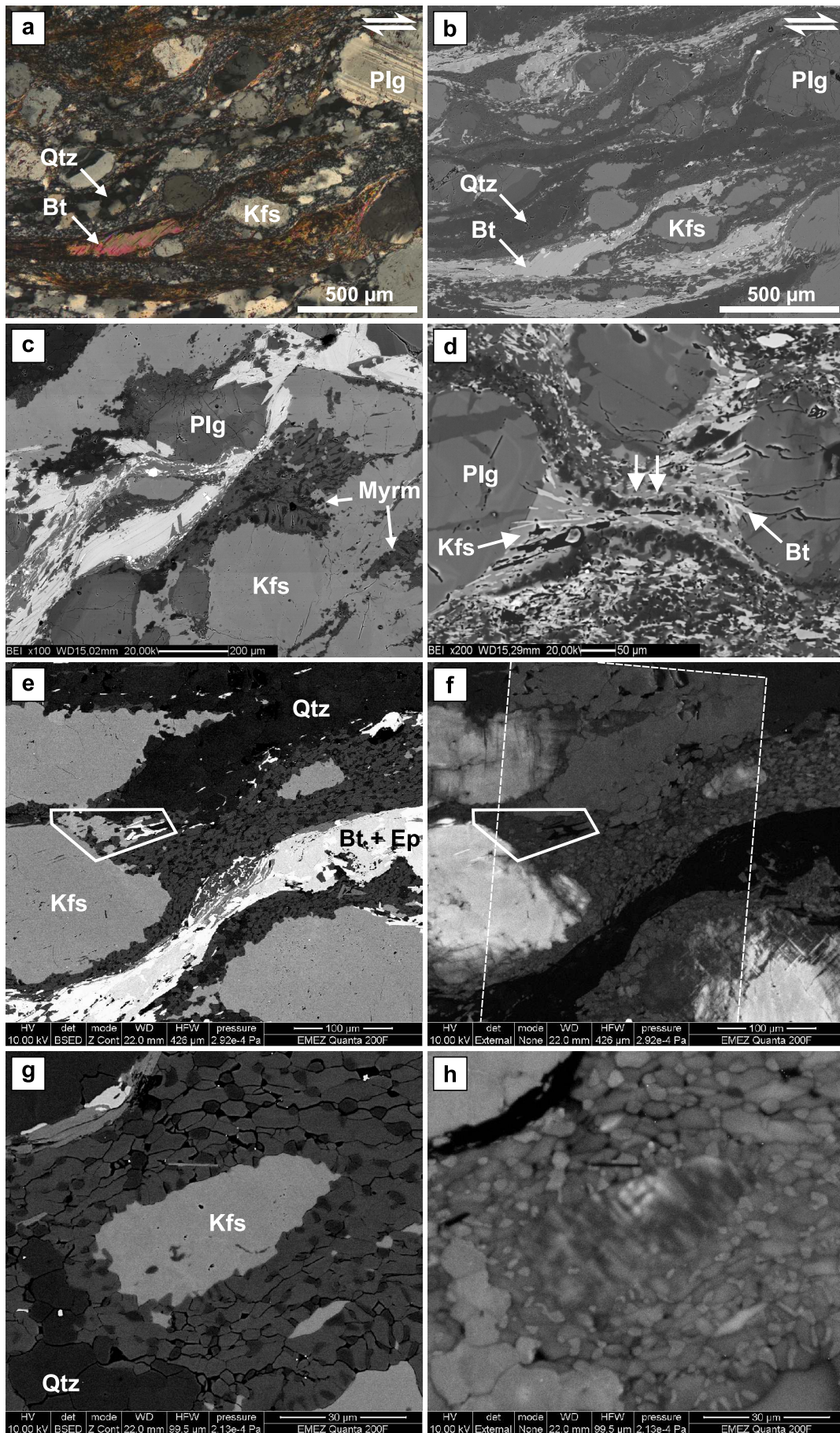


Figure 1

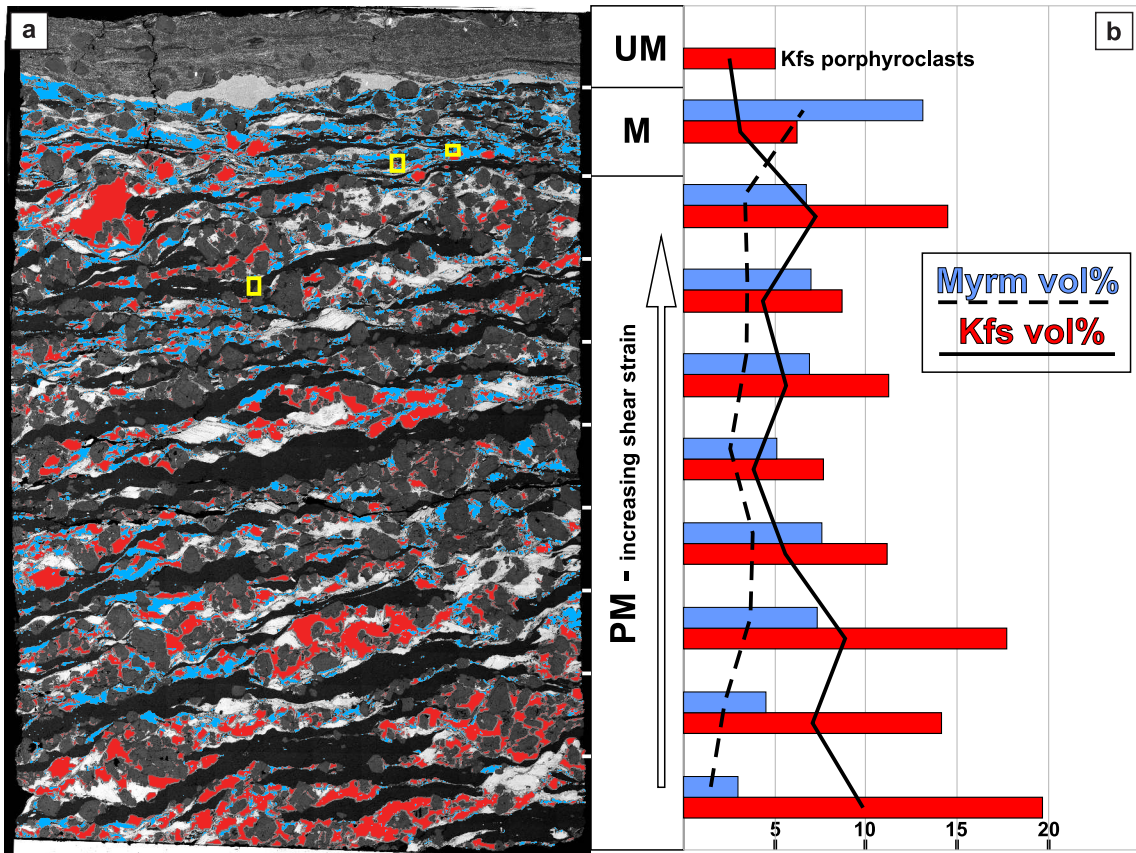


Figure 2

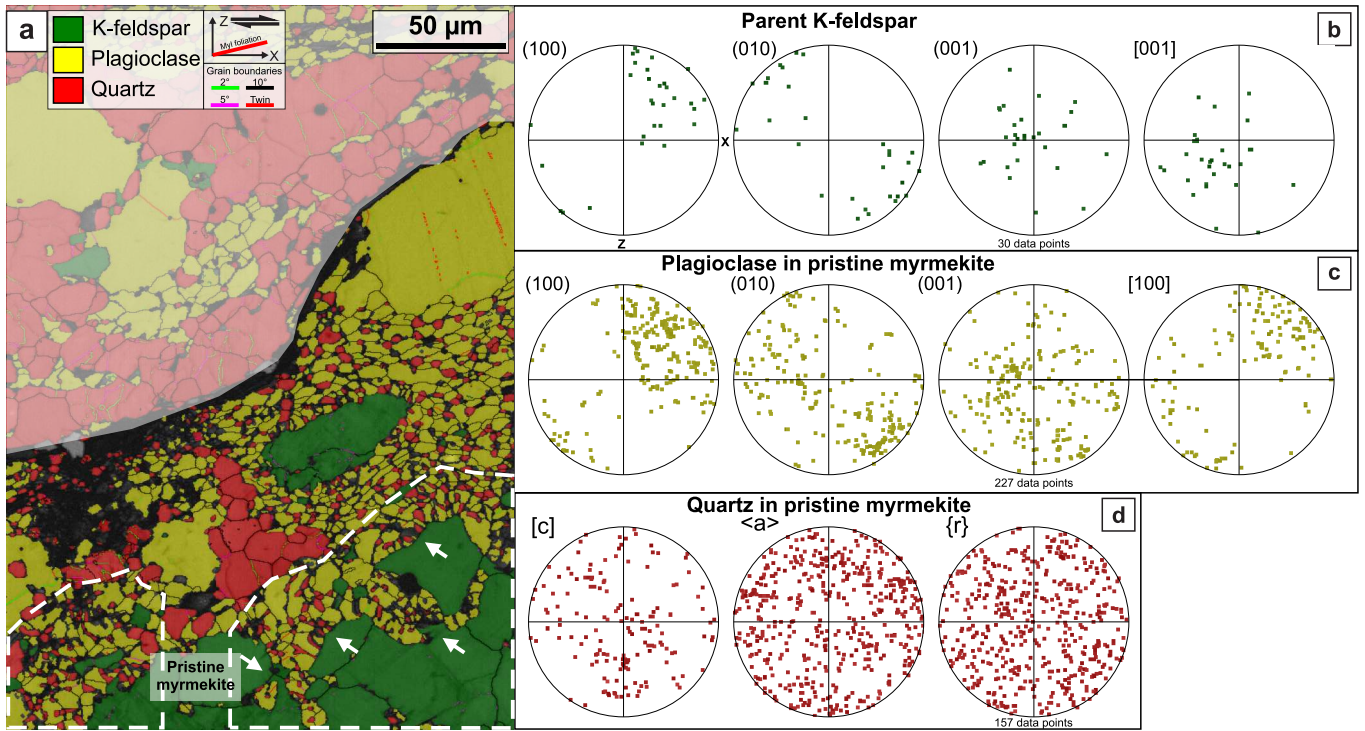


Figure 3

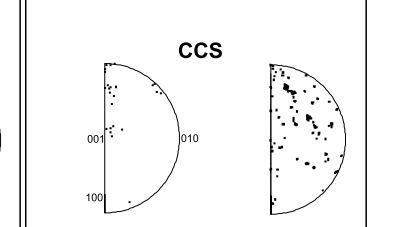
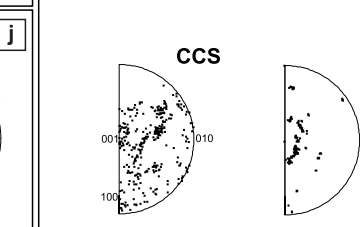
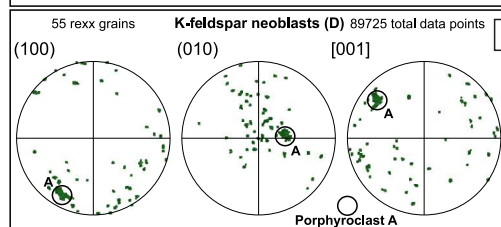
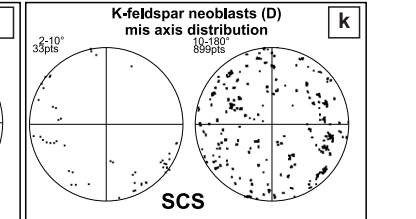
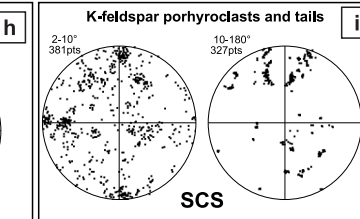
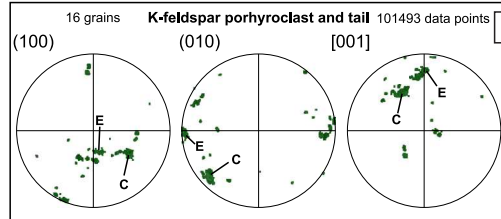
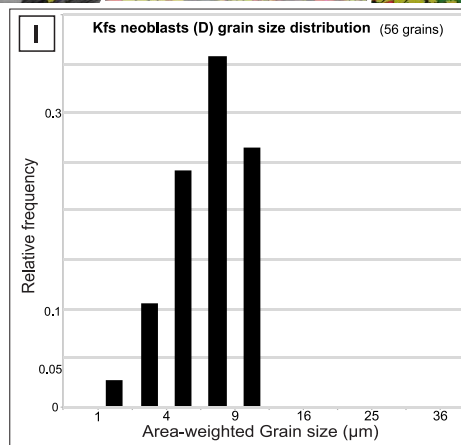
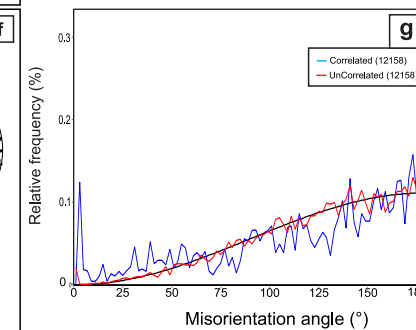
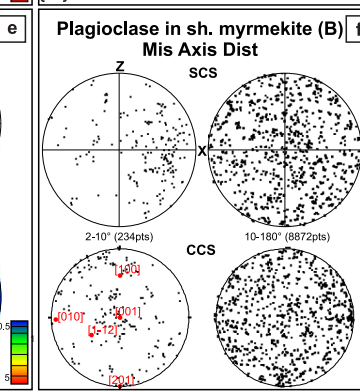
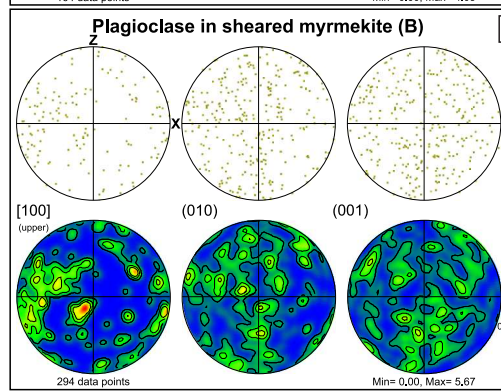
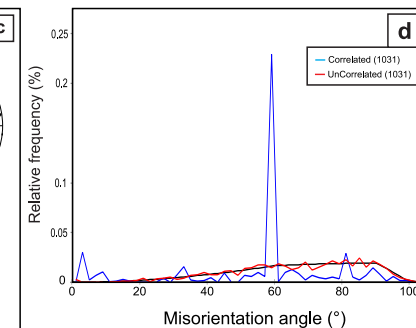
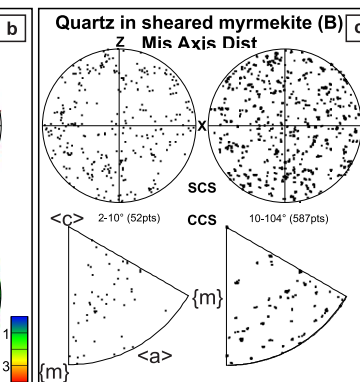
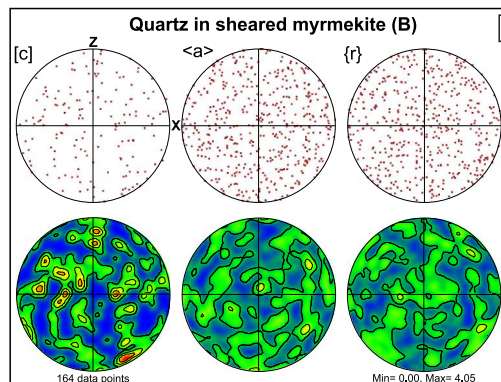
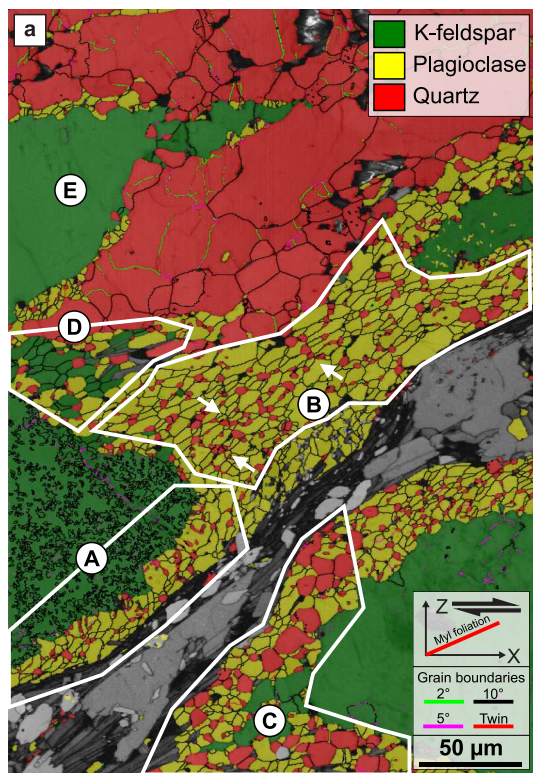


Figure 4

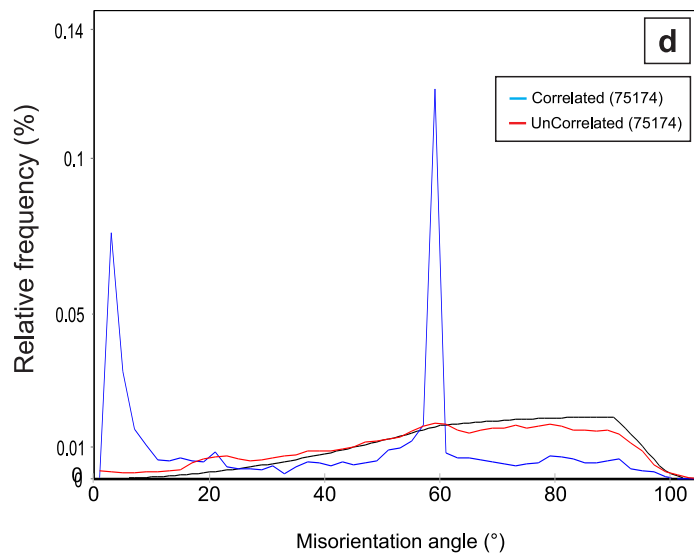
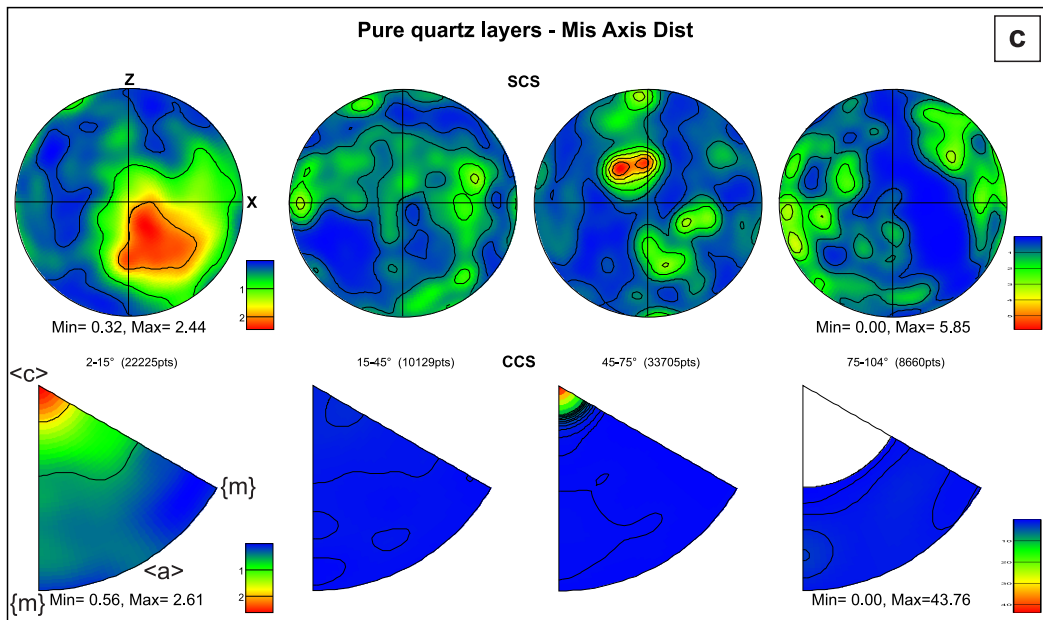
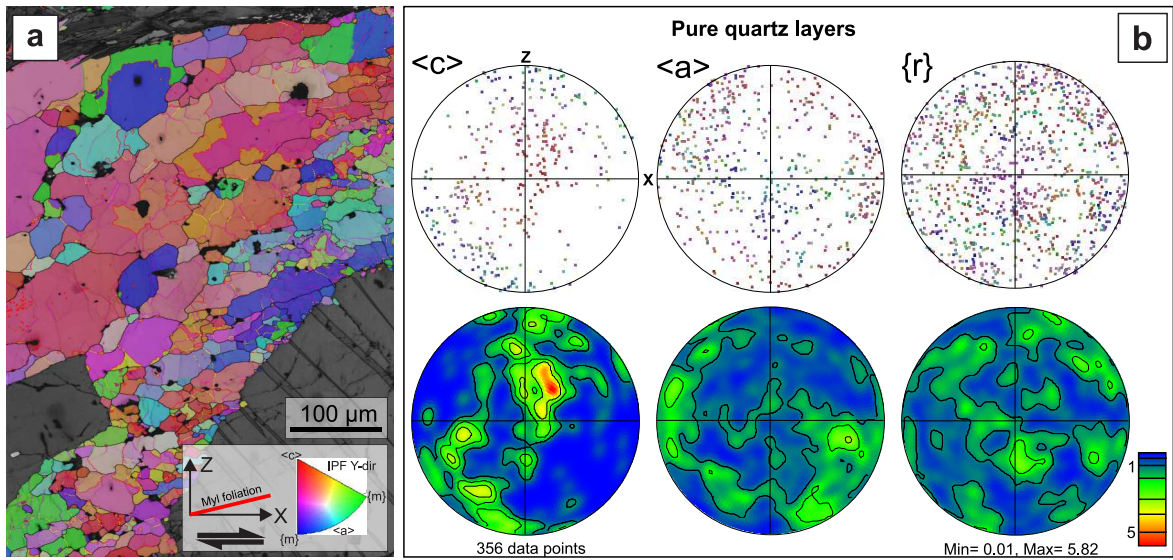


Figure 5

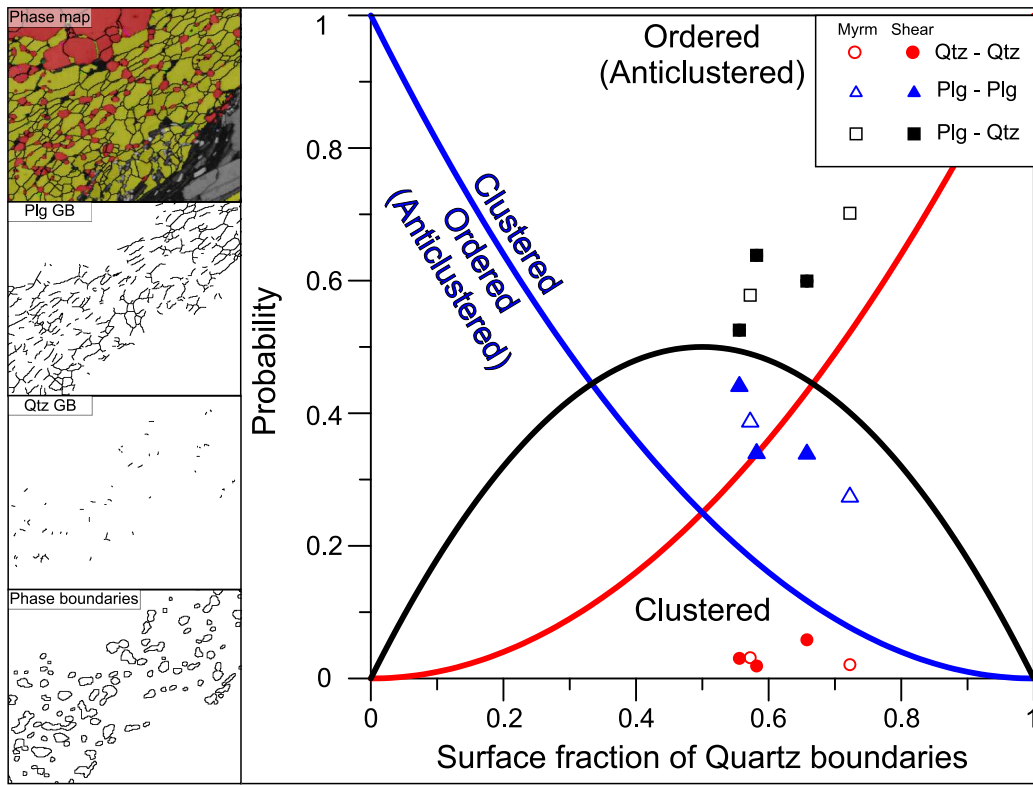


Figure 6

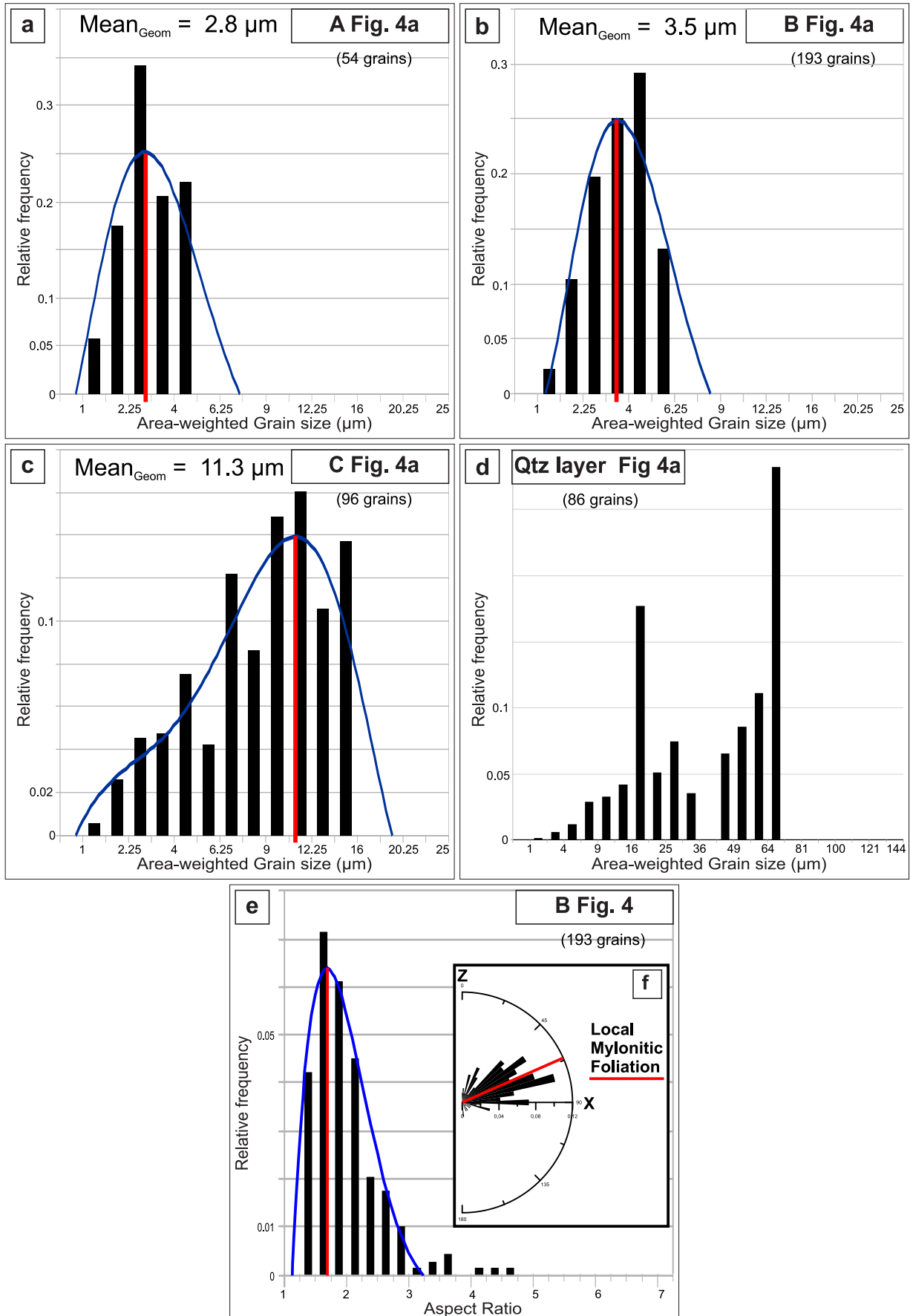


Figure 7

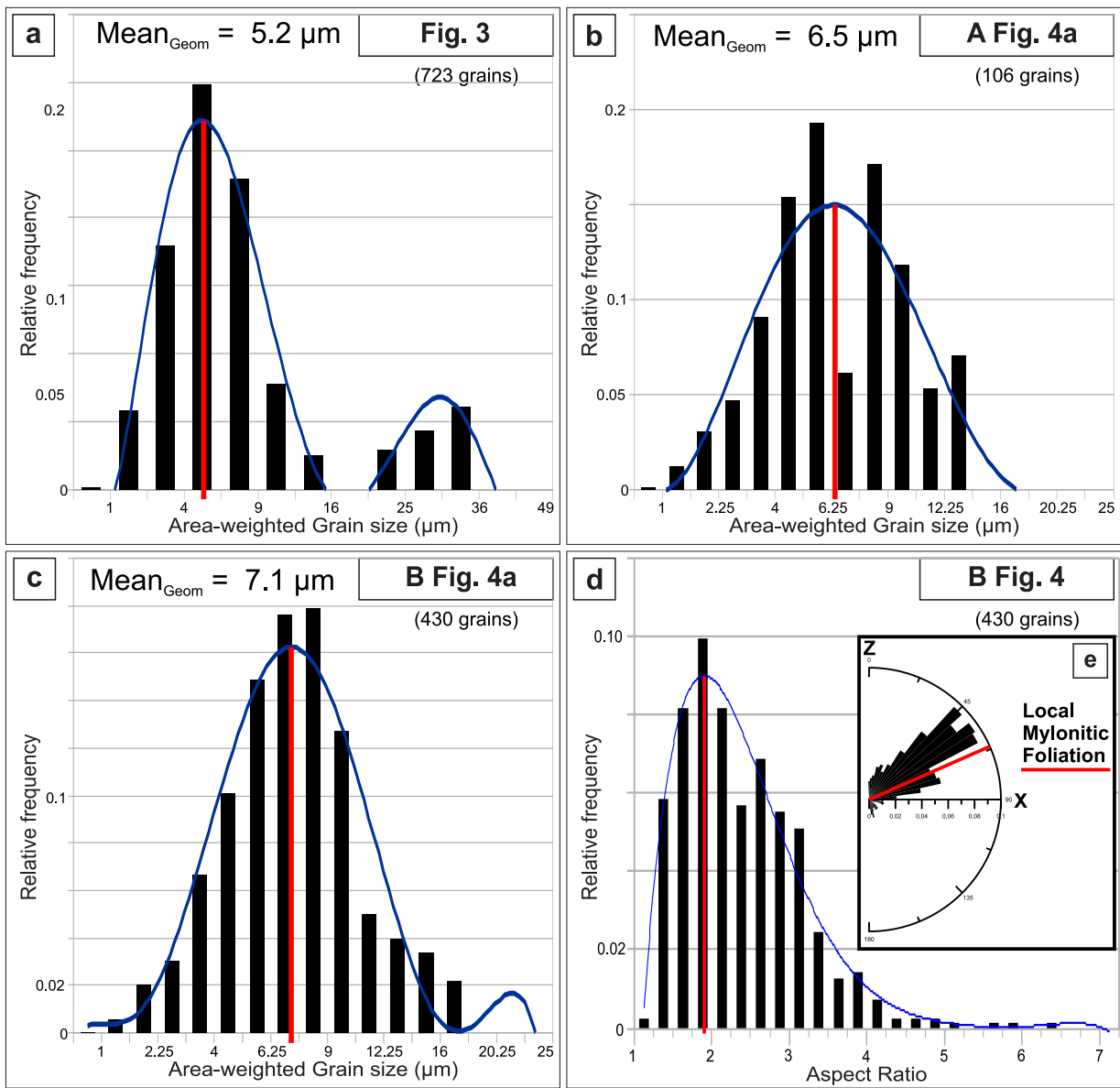


Figure 8

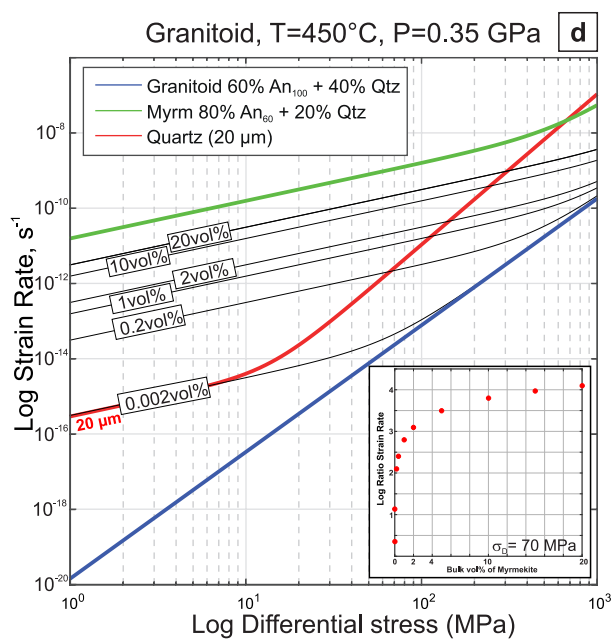
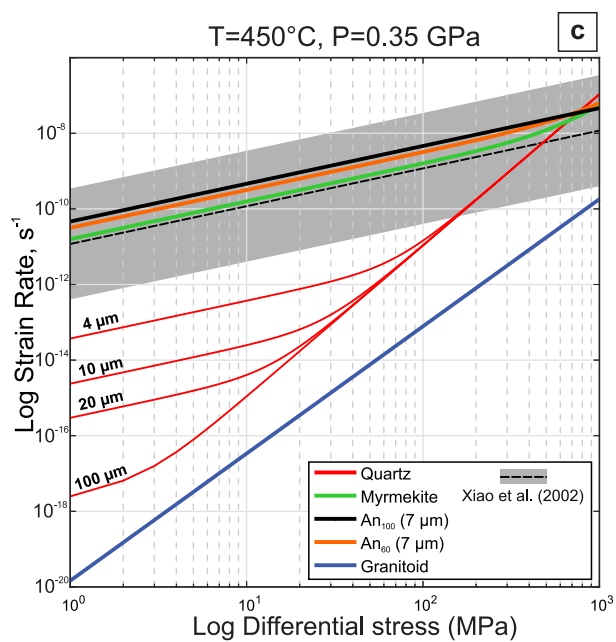
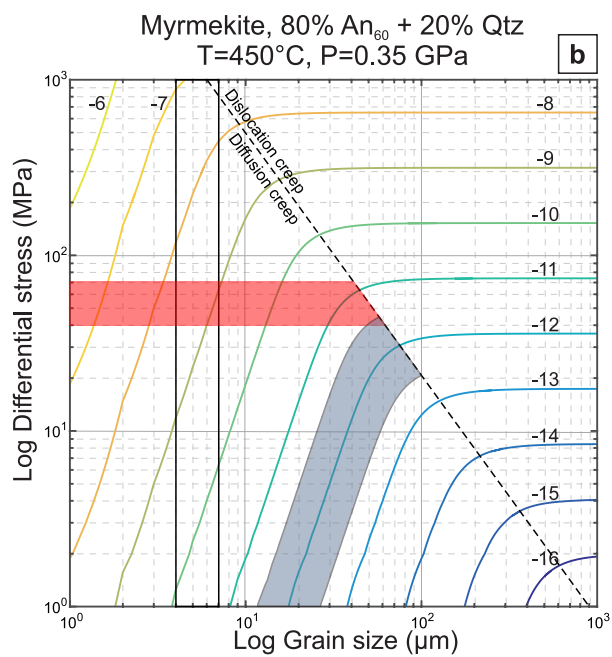
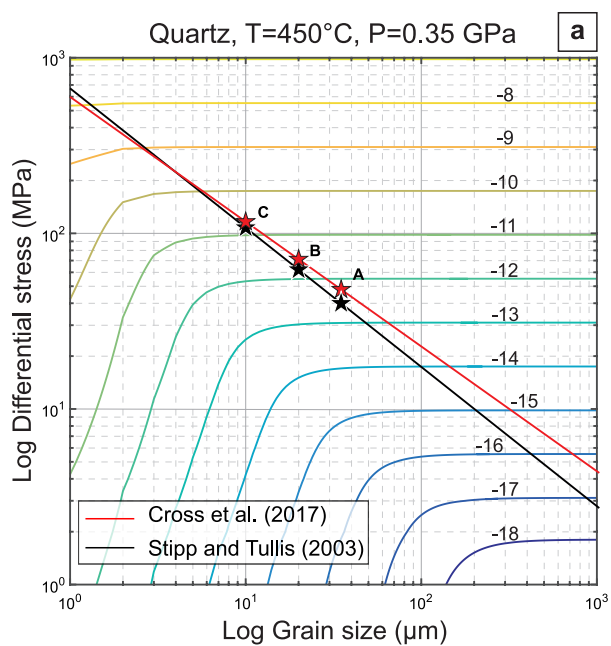


Figure 9